


RESEARCH ARTICLE

10.1029/2022MS003105

Key Points:

- Ensemble Kalman methods can be used to train parameterizations regardless of their architecture
- They enable learning from partial observations or statistics in the presence of noise
- Their effectiveness is demonstrated by calibrating an atmospheric turbulence and convection scheme

Correspondence to:

I. Lopez-Gomez,
 ilopezgo@caltech.edu

Citation:

Lopez-Gomez, I., Christopoulos, C., Langeland Ervik, H. L., Dunbar, O. R. A., Cohen, Y., & Schneider, T. (2022). Training physics-based machine-learning parameterizations with gradient-free ensemble Kalman methods. *Journal of Advances in Modeling Earth Systems*, 14, e2022MS003105. <https://doi.org/10.1029/2022MS003105>

Received 24 MAR 2022

Accepted 8 AUG 2022

Training Physics-Based Machine-Learning Parameterizations With Gradient-Free Ensemble Kalman Methods

Ignacio Lopez-Gomez¹ , Costa Christopoulos¹ , Haakon Ludvig Langeland Ervik¹, Oliver R. A. Dunbar¹ , Yair Cohen¹ , and Tapio Schneider^{1,2}

¹Department of Environmental Science and Engineering, California Institute of Technology, Pasadena, CA, USA, ²Jet Propulsion Laboratory, California Institute of Technology, Pasadena, CA, USA

Abstract Most machine learning applications in Earth system modeling currently rely on gradient-based supervised learning. This imposes stringent constraints on the nature of the data used for training (typically, residual time tendencies are needed), and it complicates learning about the interactions between machine-learned parameterizations and other components of an Earth system model. Approaching learning about process-based parameterizations as an inverse problem resolves many of these issues, since it allows parameterizations to be trained with partial observations or statistics that directly relate to quantities of interest in long-term climate projections. Here, we demonstrate the effectiveness of Kalman inversion methods in treating learning about parameterizations as an inverse problem. We consider two different algorithms: unscented and ensemble Kalman inversion. Both methods involve highly parallelizable forward model evaluations, converge exponentially fast, and do not require gradient computations. In addition, unscented Kalman inversion provides a measure of parameter uncertainty. We illustrate how training parameterizations can be posed as a regularized inverse problem and solved by ensemble Kalman methods through the calibration of an eddy-diffusivity mass-flux scheme for subgrid-scale turbulence and convection, using data generated by large-eddy simulations. We find the algorithms amenable to batching strategies, robust to noise and model failures, and efficient in the calibration of hybrid parameterizations that can include empirical closures and neural networks.

Plain Language Summary Artificial intelligence represents an exciting opportunity in Earth system modeling, but its application brings its own set of challenges. One of the challenges is to train machine learning systems within Earth system models from partial or indirect data. Here, we present algorithms, known as ensemble Kalman methods, which can be used to train such systems. We demonstrate their use in situations where the data used for training are noisy, only indirectly informative about the model to be trained, and may only become available sequentially. As an example, we present training results for a state-of-the-art model for turbulence, convection, and clouds for use within Earth system models. This model is shown to learn efficiently from data in a variety of configurations, including situations where the model contains neural networks.

1. Introduction

The remarkable achievements of machine learning over the past decade have led to renewed interest in informing Earth system models with data (Reichstein et al., 2019; Schneider et al., 2017). The spotlight is often on creating or improving models of processes that are deemed important for the correct representation of the Earth system as a whole. Examples of these processes include moist convection (Brenowitz et al., 2020), cloud microphysical and radiative effects (Meyer et al., 2022; Seifert & Rasp, 2020; Villefranque et al., 2021), and evapotranspiration (Zhao et al., 2019), among others.

Processes governed by poorly understood dynamics, such as biological processes, are obvious candidates for representation by purely data-driven models. On the other end of the spectrum are fluid transport processes, which are governed by the Navier-Stokes equations. Uncertain representation of these processes comes from a lack of resolution, not lack of knowledge about the underlying dynamics. Hybrid modeling approaches that incorporate domain knowledge and augment it by learning from data are attractive for such processes because they reduce what needs to be learned from data.

For processes with known dynamics, data-informed models fall into three broad categories according to their leverage of domain knowledge. In the first category are models that try to learn the entire dynamics using a

sufficiently expressive hypothesis set, such as deep neural networks. This approach has proved successful for predicting precipitation over short time horizons (Ravuri et al., 2021), and it has been explored for medium-range weather forecasting (Lopez-Gomez et al., 2022; Pathak et al., 2022; Rasp & Thurey, 2021). An advantage of these models is that they are typically easy to implement and cheap to evaluate. They can afford very large time steps (Weyn et al., 2021), or they may learn directly mappings from the initial state to a probability distribution of final states with no need of time marching or ensemble forecasting (Sønderby et al., 2020). A deficiency of these models is that they often require an extreme amount of data to constrain the many (often $> 10^6$) parameters in them and to achieve acceptable performance.

Methods in the second and third categories employ models of subgrid processes to solve the closure problem that arises when coarse-graining the known dynamics, which are retained. Retaining the coarse-grained equations of motion ensures conservation of mass, momentum, and energy, which is more difficult when using models in the first category (Beucler et al., 2021; Brenowitz et al., 2020). The second category encompasses methods that try to learn the functional form of these closures avoiding the use of empirical laws. For example, Zanna and Bolton (2020) use relevance vector machines to prune a library of functions, resulting in a closed form expression of mesoscale eddy fluxes in ocean simulations; Ling et al. (2016) learn a neural network closure of the Reynolds stress anisotropy tensor while explicitly encoding rotational invariance in the context of $k - \epsilon$ models of turbulence.

Finally, the third category refers to methods that seek to learn the parameters that arise in empirical closures of subgrid processes. In general, models in the third category are more restrictive, and they may be expected to underperform with respect to those in the second category given sufficient data on the target distributions. However, the limited parametric complexity of these closures makes them amenable to physical interpretation, robust to overfitting, and better suited for learning in the low-data regime. This may be attractive for Earth system models, for which online learning from limited high-resolution data may be a useful strategy to assimilate computationally generated data of the changing climate (Schneider et al., 2017).

A barrier delimiting data-driven and empirical subgrid-scale closures is the access to practical calibration tools. Neural network parameterizations are easily calibrated using stochastic gradient descent through backpropagation, which limits data sets to those including output labels, and models to those that afford automatic differentiation with respect to their parameters. Empirical closures, which may depend on time-evolving terms with memory (Lopez-Gomez et al., 2020) or yield unobservable outputs (e.g., turbulent vs. dynamical entrainment in Cohen et al. (2020)) cannot be trained using this approach. Traditional Bayesian inference techniques, like random walk Metropolis (Metropolis et al., 1953) or sequential Monte Carlo (Moral et al., 2006), can be used in this context if the number of parameters is small and the model to be trained is cheap to evaluate. Such methods additionally provide uncertainty quantification, but they become intractable for expensive models with many parameters (Cotter et al., 2013; Souza et al., 2020). Model-agnostic tools that enable fast calibration of subgrid-scale closures from diverse data are a necessary step toward the development of hybrid closures that leverage the strengths of all modeling approaches.

With this goal in mind, we present calibration strategies for models of subgrid processes, formulating the learning task as an inverse problem (Kovachki & Stuart, 2019). Solutions to the inverse problem are sought using the ensemble and unscented Kalman inversion (UKI) algorithms (Huang, Schneider, & Stuart, 2022; Iglesias et al., 2013). Emphasis is given to practical aspects of this specific inverse problem, which have not previously been explored in the literature. These include the construction of a domain-agnostic loss function from high-dimensional observations, a heuristic a priori estimate of model error, systematic handling of model failures during the training process, and the use of the Kalman inversion algorithms when only noisy evaluations of the loss function are available.

The strategies presented here are designed to have several attractive properties compared to other learning algorithms. First, framing learning as an inverse problem enables the use of partial observations or statistically aggregated data. Second, calibration is performed using gradient-free methods, which are well suited for stochastic models and/or models whose derivatives do not exist or are difficult to obtain. Finally, the strategies presented are amenable to parallelization and the use of high-dimensional correlated observations. The last two properties draw heavily on the use of Kalman inversion algorithms to tackle the inverse problem, which themselves build on the success of the ensemble Kalman filter (EnKF) for data assimilation (Burgers et al., 1998; Evensen, 1994;

Houtekamer & Mitchell, 1998) and are closely related to iterative EnKF (Bocquet & Sakov, 2013; Chen & Oliver, 2012; Emerick & Reynolds, 2013). The methods presented here are applicable to models of subgrid-scale processes, within the second and third categories described above. They provide an alternative to learning algorithms that impose stringent requirements on either the model architecture, its computational cost, or the nature of the training data.

The article is organized as follows. Section 2 casts learning about parameterizations as an inverse problem, which can be solved through the minimization of a regularized low-dimensional encoding of the data-model mismatch. Section 3 reviews the application of the ensemble and UKI algorithms to inverse problems and proposes modifications to their update equations that enable training models that may experience failures. Section 4 then applies these ensemble Kalman algorithms to the calibration of closures within an eddy-diffusivity mass-flux (EDMF) scheme of turbulence and convection, using data generated from large-eddy simulations (LES). The robustness of these learning strategies is demonstrated by calibrating the EDMF scheme using noisy loss evaluations and partial information, and their flexibility is emphasized by learning the parameters in a hybrid model containing both empirical and neural network closures. Finally, Section 5 ends with a discussion of the findings and concluding remarks.

2. Learning About Parameterizations as an Inverse Problem

We consider the problem of learning the parameters ϕ of a dynamical model $\Psi(\phi)$, using noisy observations y of the true dynamical system ζ that $\Psi(\phi)$ seeks to represent. In the context of subgrid parameterizations, $\Psi(\phi)$ represents a closed version of the coarse-grained dynamical system (e.g., the filtered Navier-Stokes equations), where closures are parameterized by ϕ . The model $\Psi(\phi)$ maps a user-defined initial state φ_0 and a forcing $F_\phi(t)$ to a state trajectory $\hat{\varphi}(t)$. Thus, our definition of $\Psi(\phi)$ can be interpreted as the iterative application of the resolvent operator on the initial field φ_0 (Brajard et al., 2021). In the following, we denote any set of initial and forcing conditions collectively as the configuration $x_c = \{\varphi_0, F_\phi\}_c$; the definition of all symbols is summarized in the appendix.

For each configuration x_c , the dynamical model can be related to the observations y_c by the observational map \mathcal{H}_c , which encapsulates all averaging and post-processing operations necessary to yield the model predictions associated with the observations. More precisely, the relationship between the observations y_c , the true dynamics ζ , and the dynamical model $\Psi(\phi)$ for a given configuration may be expressed as

$$y_c = \mathcal{H}_c \circ \zeta(x_c) + \eta_c = \mathcal{H}_c \circ \Psi(\phi; x_c) + \delta(x_c) + \eta_c, \quad (1)$$

where $\phi \in \mathbb{R}^p$ is the vector of learnable parameters, η_c is the observational noise associated with y_c , and $\delta(x_c)$ is the model or representation error, which we define as the mismatch between the denoised observations $\mathcal{H}_c \circ \zeta(x_c)$ and the output of a best-fitting model $\mathcal{H}_c \circ \Psi(\phi^*; x_c)$, following Kennedy and O'Hagan (2001). Thus, the model error is approximated as additive (Cohn, 1997; van Leeuwen, 2015) and defined with respect to the observational map \mathcal{H}_c and the optimal parameters ϕ^* that minimize its contribution to the data-model relation 1.

Observations are considered to come from finite spatial and temporal averages of fields such as temperature. Learning from averages can help prevent overfitting to trajectories in chaotic systems by focusing on the statistics of the dynamics (Morzfeld et al., 2018). It also improves numerical stability when coupling to a parent model (Brenowitz & Bretherton, 2018). Under this definition of observations, it is reasonable to assume the noise η_c to be additive and Gaussian. In the following, we will further consider $\delta(\cdot)$ to be a centered Gaussian, although this constitutes a significantly stronger assumption (i.e., that the model is unbiased) and may not be appropriate for a detailed characterization of posterior uncertainty (Brynjarsdóttir & O'Hagan, 2014; van Leeuwen, 2015). The construction of more precise error models remains a challenge beyond the scope of this work. These assumptions enable us to write $\delta(x_c) + \eta_c \sim \mathcal{N}(0, \Gamma_c)$.

In general, we are interested in minimizing the mismatch between y_c and the model output for a wide range of configurations $C = \{x_c, c = 1, \dots, |C|\}$ that are representative of the conditions in which the model will operate. This defines the global data-model relation

$$y = \mathcal{H} \circ \Psi(\phi) + \delta + \eta, \quad (2)$$

where $y = [y_1, \dots, y_{|C|}]^T \in \mathbb{R}^d$, $\delta = [\delta(x_1), \dots, \delta(x_{|C|})]^T$, $\eta = [\eta_1, \dots, \eta_{|C|}]^T$, $\mathcal{H} \circ \Psi(\phi) = [\mathcal{H}_1 \circ \Psi(\phi; x_1), \dots, \mathcal{H}_{|C|} \circ \Psi(\phi; x_{|C|})]^T$, and $\delta + \eta \sim \mathcal{N}(0, \Gamma)$. In addition, implicit in the definition of the dynamical model $\Psi(\phi)$ is a discrete resolution Δ . This dependence may be lifted if the closures are designed to be scale-aware or scale-independent, in which case the relation 2 should be augmented by stacking copies of y and evaluating $\mathcal{H} \circ \Psi(\phi, \Delta_i)$ for different discretizations Δ_i .

In practice, the parameters ϕ are often defined over some subspace $U \subset \mathbb{R}^p$ outside of which the model trajectories are unphysical or numerically unstable. Examples of these are parameters controlling the diffusion or turbulent dissipation of a scalar field, for which negative values are not physically valid. On the other hand, many algorithms designed to solve inverse problems assume $\phi \in \mathbb{R}^p$. This obstacle may be circumvented by defining a transformation $\mathcal{T} : U \rightarrow \mathbb{R}^p$, such that the global data-model relation 2 can be defined in an unconstrained parameter space,

$$y = \mathcal{G}(\theta) + \delta + \eta, \quad (3)$$

where

$$\mathcal{G} := \mathcal{H} \circ \Psi \circ \mathcal{T}^{-1}, \quad \phi = \mathcal{T}^{-1}(\theta). \quad (4)$$

In Equations 3 and 4, $\theta \in \mathbb{R}^p$ is the parameter vector in unconstrained space and $\mathcal{G} : \mathbb{R}^p \rightarrow \mathbb{R}^d$ is the map from transformed parameters to model predictions, which represents the forward model. The task of learning a set of model parameters θ under relation 3 can be cast as the Bayesian inverse problem of finding the posterior (Huang, Huang, et al., 2022; Kaipio & Somersalo, 2006; Tarantola, 2005)

$$\rho(\theta|y, \Gamma) = \frac{e^{-\mathcal{L}(\theta; y)}}{Z(y|\Gamma)} \rho_{\text{prior}}(\theta), \quad \mathcal{L}(\theta; y) = \frac{1}{2} \|y - \mathcal{G}(\theta)\|_{\Gamma}^2, \quad (5)$$

where $Z(y|\Gamma)$ is a normalizing constant, $\|\cdot\|_{\Gamma}^2$ denotes the Mahalanobis norm $\langle \cdot, \Gamma^{-1} \cdot \rangle$, \mathcal{L} is the loss or negative log-likelihood, and $\rho_{\text{prior}}(\theta)$ is the prior density. We stress that the posterior $\rho(\theta|y, \Gamma)$ is conditioned on our approximation of the noise $\delta + \eta$; see Kennedy and O'Hagan (2001) for a discussion on the usefulness and caveats of such an approach. Given the inverse problem defined by Equations 3–5, we may be interested in finding the maximum a posteriori (MAP), approximations of the density $\rho(\theta|y, \Gamma)$ around the MAP for uncertainty quantification, or simply the maximum likelihood estimator (MLE) if we have no prior information about θ . Algorithms to perform these tasks are described in Section 3.

The error covariance Γ_c appearing in each model-data relation 1, and ultimately defining the inverse problem 3–5, is yet to be defined. In Section 2.1, we suggest an estimate of Γ_c relevant to the calibration of models with an unknown error structure $\delta(\cdot)$. In addition, the choice of observational map \mathcal{H}_c may not be evident when training dynamical models that aim to represent complex dynamical systems ζ with many observable fields. Section 2.2 suggests a model-agnostic definition of \mathcal{H}_c that can be used to construct a regularized inverse problem.

2.1. Estimate of Noise Covariances

Since the structure of the representation or model error δ is unknown a priori, we must either parameterize it and calibrate it as well (Brynjarsdóttir & O'Hagan, 2014) or use a heuristic to capture its magnitude. Here, we follow the second route and offer a heuristic that has worked well for us in practice. If we take $y_c = y_c(t)$ to be an observation of the true system in configuration x_c aggregated over a time interval $[t, t + \tau]$, we can write Equation 1 as

$$y_c(t) - y_c(0) = \mathcal{H}_c \circ \Psi(\phi; x_c, t) - y_c(0) + \delta(x_c, t) + \eta_c(t). \quad (6)$$

If we further consider a model with no predictive power of the first kind (Lorenz, 1975; Schneider & Griffies, 1999), such that $\mathcal{H}_c \circ \Psi(\phi; x_c, t) \approx y_c(0)$ for all times t , the covariance of Equation 6 from $t = 0$ to $t = t_c \gg \tau$ reads

$$\Gamma_c = \text{Cov}(y_c) \approx \text{Cov}(\delta(x_c)) + \text{Cov}(\eta_c), \quad (7)$$

which yields an estimate of the aggregate noise $\eta_c + \delta(x_c) \sim \mathcal{N}(0, \Gamma_c)$ from the variability of the observation y_c over a time interval $[0, t_c]$. For non-stationary conditions or finite-time averages, Γ_c depends on t_c . Estimating the magnitude of the aggregate noise from the internal variability of the true dynamics ensures that the loss or negative log-likelihood $\mathcal{L}(\theta; y)$ penalizes models $\Psi(\phi)$ that produce unrealistic outputs, and it represents a form of error inflation if the best-fitting model is expected to outperform the aforementioned unskillful model. The heuristic 7 is most appropriate when the dynamical model $\Psi(\phi)$ is expressive enough to closely replicate the initial observations $y_c(0)$, such that any mismatch in the initial condition can be lumped together with the observation error.

2.2. Design of the Observational Map

2.2.1. Application to Problems With High-Resolution Data

High-resolution data are becoming increasingly common, from reanalysis products (Muñoz-Sabater et al., 2021), satellite imagery (Schmit et al., 2017), and partial differential equation (PDE) solvers such as LES (Shen et al., 2022). Although computationally generated and thus suffering from their own limitations (e.g., microphysical processes still need to be parameterized in LES), data from PDE solvers have some particularly desirable properties for the calibration of dynamical models:

- All variables appearing in the coarse-grained equations of motion are observable. As a consequence, the nature of the observational map \mathcal{H} used to constrain the model is largely a design choice.
- Data can be obtained systematically for all configurations x_c of interest, which may be chosen to minimize parameter uncertainty through active learning (Dunbar et al., 2022). In contrast, data drawn from physical measurements (e.g., field observations) are often sparse in the space of forcing and boundary conditions.

High-resolution data are often high-dimensional, which poses particular difficulties regarding the conditioning and tractability of linear systems of equations when solving inverse problems. The guidelines for the construction of the observational map \mathcal{H} presented here are tailored to solve these issues, with a focus on data from high-fidelity solvers.

2.2.2. Model Calibration

We define *model calibration* as the minimization of the mismatch between the observed dynamics and the dynamics induced by the model. We will use this definition to construct a domain-agnostic map \mathcal{H} . As an example, consider a system ζ with coarse-grained dynamics

$$\frac{\partial \bar{\varphi}}{\partial t} + \bar{\mathbf{v}} \cdot \nabla \bar{\varphi} + \nabla \cdot (\bar{\mathbf{v}}' \varphi') = F_\varphi, \quad (8)$$

where $\bar{(\cdot)}$ denotes spatial filtering, $(\cdot)'$ subfilter-scale fluctuations, and F_φ is the forcing. The field $\bar{\mathbf{v}}$ is prescribed and $\bar{\mathbf{v}}' \varphi'$ is the term parameterized in $\Psi(\phi)$. Let $S(t) = [\bar{\varphi}(t), \bar{\mathbf{v}}' \varphi'(t)]^T$ be the true state augmented with subgrid-scale fluxes, and $\hat{S}(t)$ the augmented state predicted by the model. For an incompressible fluid model, $S(t)$ would contain the fluid momentum, energy, and the subgrid advective fluxes of these fields.

Model calibration then entails finding the minimizer of the expected state mismatch $\mathbb{E} [\|\hat{S} - S\|]$ with respect to some norm and time interval, where the expectation is taken to allow for the calibration of stochastic models. Observations of the augmented state $S(t)$, which includes subgrid-scale fluxes, are not always available. Therefore, this definition of model calibration is representative of the ideal learning scenario. In scenarios where the full state is not observable, we will consider $S(t)$ to be an *observed state* formed by all relevant observable spatial fields.

2.2.3. Observations in Physical Space

Following our definition of model calibration, we preliminarily define the observations in the model-data relation 1 as finite-time averages of the normalized observed state s_c for a set of configurations C ,

$$\tilde{y}_c = \frac{1}{T_c} \int_{t_c - T_c}^{t_c} s_c(\tau) d\tau, \quad s_c = \begin{bmatrix} v_{c,1} \\ \dots \\ v_{c,n_c} \end{bmatrix} = \begin{bmatrix} V_{c,1}/\sigma_{c,1} \\ \dots \\ V_{c,n_c}/\sigma_{c,n_c} \end{bmatrix}, \quad c = 1, \dots, |C|, \quad (9)$$

where T_c is the averaging time, $v_{c,j} \in \mathbb{R}^{h_c}$ are the normalized spatial fields comprising s_c , $V_{c,j}$ are the components of the state S_c prior to normalization, n_c is the number of fields observed in configuration x_c , and h_c is the number of degrees of freedom of each field. As an example, the first configuration's observed state S_1 may include as fields atmospheric soundings of temperature and specific humidity ($n_1 = 2$) measured at h_1 vertical locations above the surface, and the second configuration's state S_2 may include these fields as well as horizontal velocity profiles ($n_2 = 4$), measured at h_2 different locations. Normalization of the observed state S_c is performed using the pooled time standard deviation $\sigma_{c,j}$ of each field $V_{c,j}$ with

$$\sigma_{c,j}^2 = h_c^{-1} \text{tr}[\text{Cov}(V_{c,j})]. \quad (10)$$

Covariances are computed over a time $t_c \geq T_c$ following the heuristic of Section 2.1 to capture the expected magnitude of the data mismatch,

$$\text{Cov}(V_{c,j}) = \frac{1}{t_c} \int_0^{t_c} V_{c,j} V_{c,j}^T d\tau - \frac{1}{t_c^2} \left(\int_0^{t_c} V_{c,j} d\tau \right) \left(\int_0^{t_c} V_{c,j} d\tau \right)^T. \quad (11)$$

We resort to pooled normalization, instead of normalizing each of the dimensions of the observed state S_c by their standard deviation, because some of the dimensions of the spatial fields $V_{c,j}$ may not vary with a given forcing, resulting in zero-variance components. For example, in the atmospheric boundary layer, observations of liquid water specific humidity will always be zero below the lifting condensation level.

Stacking the observations from all configurations together, the full observation vector \tilde{y} is

$$\tilde{y} = \begin{bmatrix} \tilde{y}_1 \\ \dots \\ \tilde{y}_{|C|} \end{bmatrix} \in \mathbb{R}^{\tilde{d}}, \quad \tilde{d} = \sum_{c=1}^{|C|} \tilde{d}_c = \sum_{c=1}^{|C|} n_c h_c. \quad (12)$$

Following again the heuristic in Section 2.1, the noise covariance associated with each observation vector $\tilde{y}_c \in \mathbb{R}^{\tilde{d}_c}$ is $\tilde{\Gamma}_c = \text{Cov}(s_c)$, computed as in Equation 11. Given that the noise is estimated independently for each configuration, the full noise covariance is the block diagonal matrix

$$\tilde{\Gamma} = \begin{bmatrix} \tilde{\Gamma}_1 & & 0 \\ & \ddots & \\ 0 & & \tilde{\Gamma}_{|C|} \end{bmatrix} \in \mathbb{R}^{\tilde{d} \times \tilde{d}}, \quad \tilde{\Gamma}_c = \text{Cov}(s_c) \in \mathbb{R}^{\tilde{d}_c \times \tilde{d}_c}, \quad (13)$$

where $\tilde{\Gamma}_c$ is the noise covariance matrix of configuration c .

2.2.4. Observations in a Reduced Space

Each covariance matrix $\tilde{\Gamma}_c$, possibly associated with high-dimensional observations and a finite sampling interval, is likely to be rank-deficient and have a large condition number $\kappa = \mu_{c,1}/\mu_{c,r_c}$, where $\mu_{c,i}$ is the i th largest eigenvalue of $\tilde{\Gamma}_c$ and r_c is the approximate rank of the matrix (Hansen, 1998). Numerically rank-deficient problems arise when \tilde{d}_c is greater than or equal to the number of samples used to construct $\tilde{\Gamma}_c$, or when there exist eigenvalues $\mu_{c,i}$ such that $\mu_{c,i}/\mu_{c,1} \lesssim \epsilon_m$, where ϵ_m is a measure of data or machine precision. An efficient regularization method for rank-deficient problems is to project the data from each configuration onto a lower-dimensional encoding, adding Tikhonov regularization to limit the condition number of the resulting global covariance matrix. If the lower-dimensional encoding is obtained through principal component analysis (PCA),

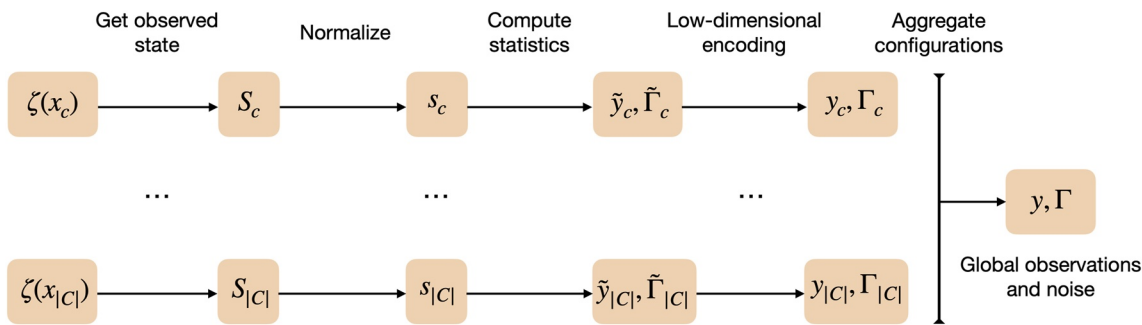


Figure 1. Schematic of the strategy used to construct a regularized inverse problem from observations of a dynamical system ζ . The two branches represent different configurations of the dynamical system. From left to right: (a) the observed state is obtained following Section 2.2.2 or from any observable fields for each configuration c ; (b) the observed state is normalized; (c) mean and covariance of the normalized state are computed; (d) \tilde{y}_c and $\tilde{\Gamma}_c$ are projected onto a lower dimension and regularized; and (e) the statistical summaries of each configuration are aggregated, defining the global inverse problem 3–5.

$$y_c = P_c^T \tilde{y}_c, \quad \Gamma_c = d_c P_c^T \tilde{\Gamma}_c P_c + \kappa_*^{-1} \mu_1 I_{d_c}, \quad (14)$$

where $y_c \in \mathbb{R}^{d_c}$ is the encoded observation vector, P_c is the projection matrix formed by the d_c leading eigenvectors of $\tilde{\Gamma}_c$, I_{d_c} is the identity matrix, μ_1 is the leading eigenvalue of the unregularized global covariance, and κ_* is the limiting condition number of the global covariance, which should be chosen to be $\kappa_* < \epsilon_m^{-1/2}$. The encoding dimension d_c should be chosen such that $d_c \leq r_c \leq \tilde{d}_c$, where r_c is the approximate rank of $\tilde{\Gamma}_c$. The actual value of d_c may be chosen through the discrepancy principle, generalized cross validation, or based on the preservation of a given fraction of the total variance, among other criteria (Hansen, 1998; Reichel & Rodriguez, 2013). The Tikhonov inflation term regularizes problems where PCA is performed between eigenvalues that are close in value, or where the range of configuration variances $\text{tr}(\tilde{\Gamma}_c)$ is large (Hansen, 1990). In projection 14, since the number of retained principal components may differ among configurations for a given truncation criterion, each block covariance matrix is scaled by d_c .

Projection 14 enables the use of arbitrarily correlated observations by regularizing the linear system $\Gamma^{-1}(\mathcal{G}(\theta) - y)$ that appears in the gradient of the loss

$$\nabla \mathcal{L}(\theta; y) \propto (D\mathcal{G}(\theta))^T \Gamma^{-1}(\mathcal{G}(\theta) - y), \quad (15)$$

and lowering its computational cost. Here, $D\mathcal{G}(\theta) \in \mathbb{R}^{d \times p}$ is the Jacobian matrix of \mathcal{G} evaluated at θ . Although the ensemble Kalman algorithms presented in Section 3 do not compute the gradient 15 explicitly, they do rely on approximations of it, so this regularization effect still applies.

Since $\tilde{\Gamma}$ in Equation 13 is block diagonal, PCA can be performed in parallel for different configurations. Projection 14 maximizes the projected variance for each configuration; it is different than performing PCA on $\tilde{\Gamma}$ in that it does not discriminate based on the total variance of each configuration. Disparities between the two approaches are discussed in Appendix A. Finally, the regularized observation vector and noise covariance matrix read

$$y = \begin{bmatrix} y_1 \\ \dots \\ y_{|C|} \end{bmatrix} \in \mathbb{R}^d, \quad \Gamma = \begin{bmatrix} \Gamma_1 & & 0 \\ & \ddots & \\ 0 & & \Gamma_{|C|} \end{bmatrix} \in \mathbb{R}^{d \times d}, \quad (16)$$

which define a regularized inverse problem of the form 3–5. A schematic of the inverse problem construction process is given in Figure 1. The construction of y_c from each dynamical system configuration $\zeta(x_c)$ defines the observational map \mathcal{H}_c , used to obtain the forward model evaluation $\mathcal{G}_c : \mathbb{R}^p \rightarrow \mathbb{R}^{d_c}$ for the same configuration from the dynamical model. The construction of each (y_c, Γ_c) pair, and the evaluation of $\mathcal{G}_c(\cdot)$, can be done in parallel.

2.3. Bayesian Interpretation of the Loss and Batching

Once the data and noise estimate encodings in Equation 16 have been defined, iterative methods to solve inverse problem 3–5 require evaluating the loss $\mathcal{L}(\theta; y)$ at each iteration, which entails running the dynamical model in all configurations C and can be very computationally demanding. A less onerous alternative is to use a mini-batch of configurations $B \subset C$ to evaluate the average configuration loss,

$$L(\theta; y_B) = \frac{1}{2|B|} \sum_{c=1}^{|B|} \|y_c - \mathcal{G}_c(\theta)\|_{\Gamma_c}^2 = \frac{1}{2} \sum_{c=1}^{|B|} \|y_c - \mathcal{G}_c(\theta)\|_{|B|\Gamma_c}^2, \quad (17)$$

which acts as a surrogate of the configuration-averaged loss $L(\theta; y) = \mathcal{L}(\theta; y)/|C|$. The use of $L(\theta; y_B)$ in lieu of $L(\theta; y)$ may be regarded as using noisy evaluations of the loss for each parameter update. From a Bayesian perspective, using $L(\theta; y)$ in Equation 5 leads to the same MAP estimator as $\mathcal{L}(\theta; y)$ but a wider uncertainty about it, since we no longer consider configurations independent. This is important when interpreting the posterior uncertainty. To employ the loss 17, we only need to use the scaling $\Gamma_c \rightarrow |B|\Gamma_c$, to approximate the aggregate loss $\mathcal{L}(\theta, y)$ when batching, we can use $\Gamma_c \rightarrow (|B|/|C|)\Gamma_c$ instead.

Batching is widely employed in data assimilation (Houtekamer & Mitchell, 2001) and deep learning, where it has been shown to help avoid convergence to local minima that generalize poorly (Keskar et al., 2016; Li et al., 2014). Understanding the behavior of algorithms when using mini-batches is crucial for online learning, where observations become available sequentially and the full loss cannot be sampled. Moreover, it provides insight into the appropriateness of training sequentially on seasonal or geographically sparse data in Earth system modeling applications. We explore the effect of batching on the solution of the inverse problem in Section 4.2, training sequentially on randomly sampled configurations with markedly different dynamics.

3. Ensemble Kalman Methods

We consider two highly parallelizable gradient-free algorithms to solve the inverse problem defined in Section 2: ensemble Kalman inversion (EKI, Iglesias et al., 2013) and (UKI, Huang, Schneider, & Stuart, 2022). Both algorithms are based on the extended Kalman filter and draw heavily on Gaussian conditioning for their derivation: underlying their update rules is the approximation of the parameter distribution as Gaussian. They afford a Bayesian interpretation when augmented with prior information at every iteration (Huang, Huang, et al., 2022); how to do this is discussed in Section 3.2. If prior information is not used, which may be desirable when training for instance neural networks, they can be regarded as derivative-free methods to obtain the MLE.

EKI and UKI have been used successfully in a wide variety of inverse problems (Huang, Schneider, & Stuart, 2022; Iglesias, 2016; Iglesias et al., 2013; Kovachki & Stuart, 2019; Xiao et al., 2016). We demonstrate them here in the context of training models that may experience numerical instabilities for a priori unknown parameter combinations, starting with a brief review of the algorithms.

3.1. Ensemble Kalman Inversion (EKI)

Ensemble Kalman inversion searches for the optimal parameter vector θ^* , given an inverse problem 3–5, through iterative updates of an initial parameter ensemble $\Theta_0 = [\theta_0^{(1)}, \dots, \theta_0^{(J)}]$, used to obtain empirical estimates of covariances between parameters and the model output at each step of the algorithm. We form the initial ensemble by randomly sampling J parameter vectors $\theta_0^{(j)} \in \mathbb{R}^p$ from a Gaussian $\mathcal{N}(m_0, \Sigma_0)$. The EKI update equation for the ensemble at iteration n is (Schillings & Stuart, 2017)

$$\Theta_{n+1} = \Theta_n + \text{Cov}(\theta_n, \mathcal{G}_n) [\text{Cov}(\mathcal{G}_n, \mathcal{G}_n) + \Delta t^{-1} \Gamma]^{-1} \varepsilon(\Theta_n), \quad (18)$$

where $\Theta_n \in \mathbb{R}^{p \times J}$, Δt is the nominal learning rate of the algorithm, and $\varepsilon(\Theta_n) \in \mathbb{R}^{d \times J}$ encodes the mismatch between the forward model evaluations and the data,

$$\varepsilon(\Theta_n) = [y_{n+1}^{(1)} - \mathcal{G}(\theta_n^{(1)}), \dots, y_{n+1}^{(J)} - \mathcal{G}(\theta_n^{(J)})], \quad (19)$$

where

$$y_{n+1}^{(j)} = y + \xi_{n+1}^{(j)}, \quad \xi_{n+1}^{(j)} \sim \mathcal{N}(0, \Delta t^{-1} \Gamma). \quad (20)$$

All covariances in Equation 18 are estimated as sample covariances of the J ensemble members,

$$\text{Cov}(\theta_n, \mathcal{G}_n) = \frac{1}{J} \left(\Theta_n - \frac{1}{J} \sum_j \theta_n^{(j)} \mathbf{1}^T \right) \left(\mathcal{G}_{\Theta_n} - \frac{1}{J} \sum_j \mathcal{G}(\theta_n^{(j)}) \mathbf{1}^T \right)^T, \quad (21)$$

$$\text{Cov}(\mathcal{G}_n, \mathcal{G}_n) = \frac{1}{J} \left(\mathcal{G}_{\Theta_n} - \frac{1}{J} \sum_j \mathcal{G}(\theta_n^{(j)}) \mathbf{1}^T \right) \left(\mathcal{G}_{\Theta_n} - \frac{1}{J} \sum_j \mathcal{G}(\theta_n^{(j)}) \mathbf{1}^T \right)^T, \quad (22)$$

where $\mathcal{G}_{\Theta_n} = [\mathcal{G}(\theta_n^{(1)}), \dots, \mathcal{G}(\theta_n^{(J)})]$, and $\mathbf{1} \in \mathbb{R}^J$ is the all-ones vector. Note that the sample covariances 21 and 22 have at most ranks $\min(\min(d, p), J - 1)$ and $\min(d, J - 1)$, respectively. From Equations 14 and 16, $\text{rank}(\Gamma) = d$ by construction, so the linear system in Equation 18 is well-defined even for $J < d$.

Through iterative application of the update 18, the ensemble Θ minimizes the projection of the model-data mismatch on the linear span of its J members. In this study, we limit the use of EKI and UKI to the calibration of dynamical models for which using an ensemble size $J \sim p$ is feasible. For models with a large number of parameters, localization or sampling error correction techniques can be used to maintain performance with $J \ll p$ members (Lee, 2021; Tong & Morzfeld, 2022), like in EnKF for data assimilation (Anderson, 2012). The update 18 also drives the ensemble toward consensus, in the sense that $|\text{Cov}(\theta_n, \mathcal{G}_n)| \rightarrow 0$ as $n \rightarrow \infty$; a popular method to control collapse speed is additive inflation (Anderson & Anderson, 1999; Tong & Morzfeld, 2022). This collapse property precludes obtaining information about parameter uncertainties directly from EKI. However, the sequence of parameter-output pairs $\{\Theta_n, \mathcal{G}_{\Theta_n}\}$ can be used to train emulators for uncertainty quantification (Cleary et al., 2021).

3.1.1. Addressing Model Failures Within the Ensemble

For some parameters θ_p , simulations may be physically or numerically unstable. For instance, the Courant–Friedrichs–Lewy condition in fluid solvers may change nonlinearly with model parameters, or the initialized weights from a neural network parameterization may lead to unstable trajectories. In such situations, we need to modify Equation 18 to account for model failures within the ensemble.

Here, we propose a novel failsafe EKI update based on the successful parameter ensemble. Let $\Theta_{s,n} = [\theta_{s,n}^{(1)}, \dots, \theta_{s,n}^{(J_s)}]$ be the successful ensemble, for which each evaluation $\mathcal{G}(\theta_{s,n}^{(j)})$ is stable or physically consistent, and let $\theta_{f,n}^{(k)}$ be the ensemble members for which the evaluation of the forward model $\mathcal{G}(\theta_{f,n}^{(k)})$ fails. We update the successful ensemble $\Theta_{s,n}$ to $\Theta_{s,n+1}$ using Equation 18, and redraw each failed ensemble member from a Gaussian defined by the successful ensemble

$$\theta_{f,n+1}^{(k)} \sim \mathcal{N}(m_{s,n+1}, \Sigma_{s,n+1}), \quad (23)$$

where

$$m_{s,n+1} = \frac{1}{J_s} \sum_{j=1}^{J_s} \theta_{s,n+1}^{(j)}, \quad \Sigma_{s,n+1} = \text{Cov}(\theta_{s,n+1}, \theta_{s,n+1}) + \kappa_*^{-1} \mu_{s,1} I_p \quad (24)$$

are the sample mean and regularized sample covariance matrix of the updated successful ensemble. In Equation 24, κ_* is a limiting condition number and $\mu_{s,1}$ is the largest eigenvalue of the sample covariance $\text{Cov}(\theta_{s,n+1}, \theta_{s,n+1})$. This update has proved very effective for us in practice, even in situations where $J_s < J/2$; we use it throughout Section 4. The failsafe update may be combined with other conditioning techniques at initialization. For instance, the initial ensemble Θ_0 may be drawn recursively until the number of failed members is reduced below an acceptable threshold.

3.2. Bayesian Regularization in Ensemble Kalman Methods

EKI implicitly regularizes the inverse problem by searching for the optimal solution θ^* over the finite-dimensional space spanned by the initial ensemble. Although UKI does not share this property, both algorithms can be equipped with Bayesian regularization by considering the augmented data-model relation (Chada et al., 2020)

$$y_a = \mathcal{G}_a(\theta) + \xi := \begin{bmatrix} y \\ m_p \end{bmatrix} = \begin{bmatrix} \mathcal{G}(\theta) \\ \theta \end{bmatrix} + \begin{bmatrix} \hat{\delta} + \hat{\eta} \\ \lambda \end{bmatrix}, \quad (25)$$

instead of Equation 3. Here, $m_p \in \mathbb{R}^p$ is the parameter prior mean, $\lambda \sim \mathcal{N}(0, 2\Lambda)$ defines the degree of regularization, $\hat{\delta} + \hat{\eta} \sim \mathcal{N}(0, 2\Gamma)$, and $\xi \sim \mathcal{N}(0, \Gamma_a)$ is the augmented error defined by Equation 25. In practice, using Equation 25 amounts to substituting $\{\mathcal{G}, y, \Gamma\}$ by $\{\mathcal{G}_a, y_a, \Gamma_a\}$ in both algorithms. The Kalman inversion solution to the inverse problem defined by Equation 25 then satisfies

$$\theta^* = \arg \min_{\theta} \left[\mathcal{L}(\theta; y) + \frac{1}{2} \|\theta - m_p\|_{\Lambda}^2 \right]. \quad (26)$$

From a Bayesian perspective, the solution 26 approximately maximizes the posterior density in Equation 5 for the Gaussian prior $\rho_{\text{prior}} \sim \mathcal{N}(0, \Lambda)$. This is particularly interesting for UKI, which provides parametric uncertainty estimates (Huang, Huang, et al., 2022). When using a nominal learning rate $\Delta t \neq 1$, the scaling $\Lambda \rightarrow \Delta t \cdot \Lambda$ must be used to retain the Bayesian interpretation of Λ as the prior variance, due to the fact that Δt effectively modifies the noise in Equation 18 to be $\Delta^{-1}\Gamma$. As noted before, if the original data-model relation 3 is used instead of the augmented relation 25, UKI and EKI provide MLE.

3.3. Unscented Kalman Inversion (UKI)

Unscented Kalman inversion seeks a Gaussian approximation of the posterior $\rho(\theta|y, \Gamma)$ around the MAP (given Equation 25), or an approximation of the likelihood around the MLE (given Equation 3), by deterministically evolving an initial Gaussian estimate $\mathcal{N}(m_0, \Sigma_0)$ through updates

$$m_{n+1} = m_n + \text{Cov}_q(\theta_n, \mathcal{G}_n) \left[\text{Cov}_q(\mathcal{G}_n, \mathcal{G}_n) + \Delta t^{-1}\Gamma \right]^{-1} \varepsilon(m_n), \quad (27)$$

$$\Sigma_{n+1} = (1 + \Delta t)\Sigma_n - \text{Cov}_q(\theta_n, \mathcal{G}_n) \left[\text{Cov}_q(\mathcal{G}_n, \mathcal{G}_n) + \Delta t^{-1}\Gamma \right]^{-1} \text{Cov}_q(\theta_n, \mathcal{G}_n)^T, \quad (28)$$

where m_n and Σ_n are the mean and covariance estimates of the Gaussian after n iterations of the algorithm, and $\varepsilon(m_n) = y - \mathcal{G}(m_n)$ is the data-model mismatch of the mean estimate. The covariances $\text{Cov}_q(\theta_n, \mathcal{G}_n)$ and $\text{Cov}_q(\mathcal{G}_n, \mathcal{G}_n)$ in Equations 27 and 28 are computed through quadratures over $2p + 1$ sigma points defined as

$$\hat{\theta}_n^{(j)} = m_n + a\sqrt{p} \left[\sqrt{\Sigma_n(1 + \Delta t)} \right]_j, \quad 1 \leq j \leq p, \quad (29)$$

$$\hat{\theta}_n^{(j+p)} = m_n - a\sqrt{p} \left[\sqrt{\Sigma_n(1 + \Delta t)} \right]_j, \quad 1 \leq j \leq p,$$

where $[\sqrt{\Gamma}]_j$ is the j th column of the Cholesky factor of Γ , $a = \min(\sqrt{4/p}, 1)$ is a hyperparameter defined in Huang, Schneider, and Stuart (2022), and $\hat{\theta}_n^{(0)} = m_n$ is the central sigma point. The quadratures are then defined as

$$\text{Cov}_q(\theta_n, \mathcal{G}_n) = \sum_{j=1}^{2p} w_j (\hat{\theta}_n^{(j)} - m_n) (\mathcal{G}(\hat{\theta}_n^{(j)}) - \mathcal{G}(m_n))^T, \quad (30)$$

$$\text{Cov}_q(\mathcal{G}_n, \mathcal{G}_n) = \sum_{j=1}^{2p} w_j (\mathcal{G}(\hat{\theta}_n^{(j)}) - \mathcal{G}(m_n)) (\mathcal{G}(\hat{\theta}_n^{(j)}) - \mathcal{G}(m_n))^T, \quad (31)$$

where $w_j = (2a^2 p)^{-1}$ are the quadrature weights.

A limitation of this algorithm is that the number of sigma points scales linearly with p , which precludes its use when training models with a large number of parameters. However, for situations where using an ensemble of $2p + 1$ members is tractable, UKI improves upon EKI by providing uncertainty quantification, instead of collapsing to a point estimate. In particular, when updates 27 and 28 are applied to the augmented data-model relation 25, UKI ensures that Σ_n in the limit $n \rightarrow \infty$ converges toward a Gaussian estimate of parametric uncertainty (Huang, Schneider, & Stuart, 2022),

$$\Sigma_\infty \approx \text{Cov}_q(\theta_\infty, \mathcal{G}_{a,\infty}) [\Delta t \cdot \text{Cov}_q(\mathcal{G}_{a,\infty}, \mathcal{G}_{a,\infty}) + \Gamma_a]^{-1} \text{Cov}_q(\theta_\infty, \mathcal{G}_{a,\infty})^T, \quad (32)$$

which involves the augmented forward model $\mathcal{G}_a(\cdot)$ and covariance Γ_a defined in Section 3.2. Σ_∞ approximates the covariance of the posterior in Equation 5 around m_∞ if the full loss is evaluated at every UKI iteration and $\Delta t = 1$ (Huang, Huang, et al., 2022). When batching, an equivalent approximation can be recovered by using $\Delta t = |C|/|B|$ to compensate for sampling errors in the construction of the empirical covariances 30 and 31; this is demonstrated in Section 4.2.

Finally, note that the limit 32 does not depend on Σ_0 , only on the Bayesian prior covariance Λ . This enables using a tight initial guess (i.e., $\text{tr}(\Sigma_0) \ll \text{tr}(\Lambda)$), which can reduce the fraction of model failures within the ensemble. To ensure robustness to the model failures that may still arise, we propose a modification of the UKI dynamics robust to model failures, similar to the one proposed for EKI, in Appendix B.

4. Application to an Atmospheric Subgrid-Scale Model

In this section, the framework and algorithms discussed in Sections 2 and 3 are used to learn closure parameters within an EDMF scheme of atmospheric turbulence and convection. The EDMF scheme is derived by spatially filtering the Navier-Stokes equations for an anelastic fluid, and then decomposing the subgrid flow into $n > 1$ distinct subdomains with moving boundaries (Cohen et al., 2020). In practice, the subdomain decomposition requires the use of $n - 1$ additional equations per grid-mean prognostic field, and $n - 1$ additional equations tracking the volume fraction of each subdomain within the grid (Tan et al., 2018). We retain second-order moments for one of the subdomains, the environment. Covariances within the other subdomains (updrafts) are neglected, which circumvents the need for turbulence closures therein. In the end, the EDMF equations require closure for the turbulent diffusivity and dissipation in the environment, and the mass, momentum, and tracer fluxes between environment and updrafts. In what follows, we consider an EDMF scheme with a single updraft ($n = 2$).

We consider the EDMF scheme discussed in Cohen et al. (2020); Lopez-Gomez et al. (2020), which is implemented in a single-column model (SCM). Within this SCM, we first seek to learn 16 closure parameters: Five describing turbulent mixing, dissipation, and mixing inhibition by stratification (Lopez-Gomez et al., 2020), three describing the momentum exchange between subdomains (He et al., 2021), seven describing entrainment fluxes between updrafts and the environment (Cohen et al., 2020), and another one defining the surface area fraction occupied by updrafts. In Section 4.4, we substitute the empirical dynamical entrainment closure proposed in Cohen et al. (2020) by a neural network, and train the resulting physics-based machine-learning model.

To showcase the versatility of the algorithms, UKI is used for approximate Bayesian inference of empirical parameters (using relation 25), and EKI is used for both MAP estimation of empirical parameters (relation 25, Sections 4.2, 4.3) and MLE estimation of neural network parameters (relation 3, Section 4.4). In all cases, we employ our failsafe modifications of the algorithms (Section 3.1.1 and Appendix B). The name, prior range U , and reference to the definition of each empirical parameter in the literature are given in Table 1. The prior mean is taken to be equal to the parameter values used in Lopez-Gomez et al. (2020) and Cohen et al. (2020). The prior in unconstrained space $\mathcal{N}(m_p, \Lambda)$ is obtained from the physical prior mean and range through transformations defined in Appendix C. Finally, we initialize EKI ensembles from the prior, $\mathcal{N}(m_0, \Sigma_0) \equiv \mathcal{N}(m_p, \Lambda)$, and all UKI sigma points from a tighter initial guess $\mathcal{N}(m_p, \Lambda/16)$ to demonstrate the ability of UKI to decouple from the initial guess.

4.1. Description of LES Data and Model Configurations

The data used for training and testing the EDMF scheme are taken from the LES library described in Shen et al. (2022). This library contains high-resolution simulations of low-level clouds spanning the

Table 1
Parameters ϕ Considered for Calibration in This Study

Symbol	Description	Prior range	Prior mean
c_m	Eddy viscosity coefficient	(0.01, 1.0)	0.14, LG2020
c_d	Turbulent dissipation coefficient	(0.01, 1.0)	0.22, LG2020
c_b	Static stability coefficient	(0.01, 1.0)	0.63, LG2020
$Pr_{t,0}$	Neutral turbulent Prandtl number	(0.5, 1.5)	0.74, LG2020
κ_*	Ratio of rms turbulent velocity to friction velocity	(1.0, 4.0)	1.94, LG2020
c_e	Entrainment rate coefficient	(0, 1)	0.13, C2020
c_δ	Detrainment rate coefficient	(0, 1)	0.51, C2020
c_γ	Turbulent entrainment rate coefficient	(0, 10)	0.075, C2020
β	Detrainment relative humidity power law	(0, 4)	2.0, C2020
μ_0	Entrainment sigmoidal activation parameter	(10^{-6} , 10^{-2})	$4 \cdot 10^{-4}$, C2020
χ_i	Updraft-environment buoyancy mixing ratio	(0, 1)	0.25, C2020
c_λ	Turbulence-induced entrainment coefficient	(0, 10)	0.3, C2020
a_s	Updraft surface area fraction	(0.01, 0.5)	0.1, C2020
α_b	Updraft virtual mass loading coefficient	(0, 10)	0.12, H2021
α_a	Updraft advection damping coefficient	(0, 100)	0.001, H2021
α_d	Updraft drag coefficient	(0, 50)	10.0, H2021

Note. The prior mean values are taken from LG2020 (Lopez-Gomez et al., 2020), C2020 (Cohen et al., 2020), and H2021 (He et al., 2021), where a physical description of the parameters may be found.

stratocumulus-to-cumulus transition in the East Pacific Ocean. The large-scale forcing used for these simulations is derived from the cfSites output of the HadGEM2-A model, retrieved from the Coupled Model Intercomparison Project Phase 5 archive. In particular, the monthly climatology of the cfSites output is computed over the 5-year period 2004–2008, and used to initialize and force LES for a period of 6 days. Radiative forcing is computed interactively using the Rapid Radiative Transfer Model (Mlawer et al., 1997).

The SCM runs are initialized from the coarse-grained LES fields after 5.75 days of simulation and are run for 6 hr. This runtime was chosen to be much longer than the equilibration time of the SCM to the steady forcing; experiments using a runtime of 12 hr resulted in no statistical changes of the results. Large-scale forcing is identical to that of the LES, and the radiative heating rates are given by the horizontal mean of the rates experienced by the high-resolution simulations. The observational map used to define the inverse problem follows the guidelines of Section 2.2, using time and horizontally averaged vertical profiles from the last $T_c = 3$ hr of simulation, at a vertical resolution of $\Delta z = 50$ m; this is also the resolution of the SCM simulations, which employ 80 vertical levels. Following the strategy in Figure 1, we extract the observations from each configuration as

$$S_c = \left[\bar{u}, \bar{v}, \bar{s}, \bar{q}_l, \bar{q}_t, \bar{w'q'_t}, \bar{w's'} \right]^T, \quad (33)$$

where $\bar{(\cdot)}$ denotes horizontal averaging, \bar{u} and \bar{v} are the horizontal velocity components, \bar{s} is the entropy, \bar{q}_l is the total specific humidity, $\bar{w'q'_t}$ and $\bar{w's'}$ are vertical fluxes of moisture and entropy, and \bar{q}_t is the liquid water specific humidity. The pooled variances for normalization and covariance matrix $\bar{\Gamma}_c$ associated with the observed state S_c are obtained from the full 6-day statistics of the LES to capture the internal variability of the system. Finally, a low-dimensional encoding is obtained from the normalized time-averaged observations through truncated PCA as in Equation 14, truncating the dimension of the noise covariance matrix so as to preserve 99% of the total noise variance. Calibration results using fewer observed fields at a coarser resolution are discussed in Section 4.3.

As training data, we include a total of 60 LES configurations from the Atmospheric Model Intercomparison Project (AMIP) experiment, spanning the months of January, April, July, and October, and locations from the

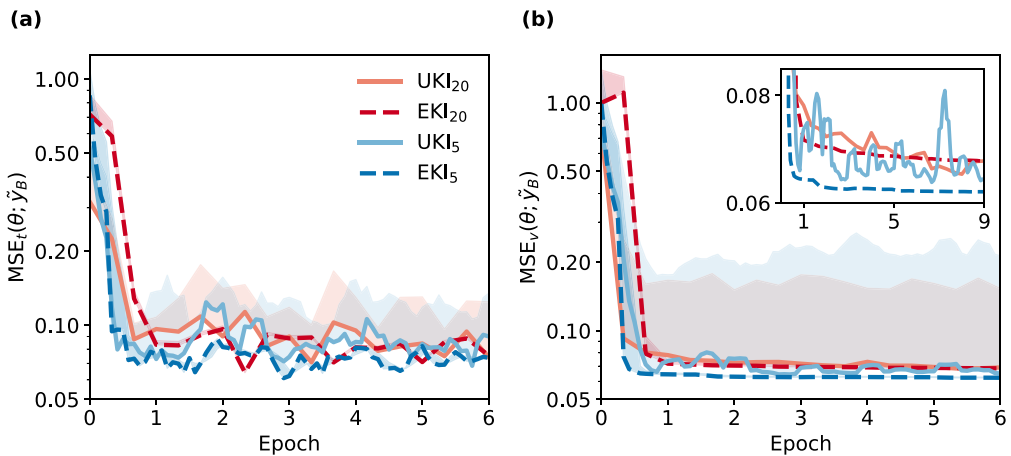


Figure 2. Batch (a) training and (b) validation MSE as defined in Equation 34. The lines represent the error of the ensemble mean $\bar{\theta}$, $\text{MSE}(\bar{\theta}; \tilde{y}_B)$, and the shading represents the ensemble standard deviation of $\text{MSE}(\theta; \tilde{y}_B)$ around the optimal point estimate $\bar{\theta}$. All errors are normalized with respect to the largest initial $\text{MSE}_v(\bar{\theta}; \tilde{y}_B)$, so they can be compared. Results are shown for ensemble and unscented Kalman inversion, using $J = 2p + 1$ and training batch sizes $|B| = 5, 20$. Errors for $|B| = 5$ are averaged using a rolling mean of 20 configurations to enable comparison with $|B| = 20$. In (b), the inset focuses on the validation error evolution for a longer training period.

coasts of Peru and California to the tropical Pacific. Results are also shown for a validation set, which includes January and July simulations from an AMIP4K experiment, where sea surface temperature is increased by 4 K with respect to AMIP. This temperature increase leads to 10%–20% weaker large-scale subsidence, higher cloud tops, and reduced cloud cover; see Shen et al. (2022) for a detailed comparison. Validation results are representative of the generalizability of the trained model for the simulation of a warming climate; the model was not trained on these warmer conditions.

4.2. Calibration Using Mini-Batch Loss Evaluations

To demonstrate the effectiveness of Kalman inversion in settings where evaluating all configurations of interest per iteration may be too expensive or impossible (e.g., due to sequential data availability), we present calibration results using mini-batches. Batching introduces noise in the loss evaluations due to sampling error. For this reason, the behavior of Kalman inversion algorithms using mini-batches is representative of their robustness to other sources of noise, such as noise in the data or stochasticity of the dynamical model. To correct for sampling noise due to batching, we use $\Delta t = |C|/|B|$ as discussed in Section 3.3.

For training, data are fed to the algorithm by drawing $|B|$ configurations randomly and without replacement from the training set at every iteration. Configurations are reshuffled at the end of every epoch (i.e., every full pass through the training set). Figure 2 shows the evolution of the training and validation errors for UKI and EKI, using training batches of 5 and 20 configurations. Since the total number of configurations in the training set is 60, an epoch requires 12 iterations when using $|B| = 5$ and 3 when using $|B| = 20$. For many geophysical applications, the cost of evaluating an ensemble of long-term statistics $\mathcal{G}(\cdot)$ from a forward model is significantly higher than performing the inversion updates 18 or 27. In these situations, a training epoch has similar computational cost for any value of $|B|$.

The training error is evaluated in normalized physical space with respect to the current batch,

$$\text{MSE}(\theta; \tilde{y}_B) = \frac{1}{\tilde{d}_B} \|\tilde{y}_B - \tilde{\mathcal{G}}_B(\theta)\|^2 = \frac{1}{\sum_{c=1}^{|B|} \tilde{d}_c} \sum_{c=1}^{|B|} \|\tilde{y}_c - \tilde{\mathcal{G}}_c(\theta)\|^2, \quad (34)$$

where $\tilde{y}_B \in \mathbb{R}^{\tilde{d}_B}$. The validation error is defined similarly, but it is computed over the entire validation set at every iteration. Thus, variations in the validation error are only due to changes in the model parameters; there is no random data sampling. The training and validation errors decrease sharply during the first epoch

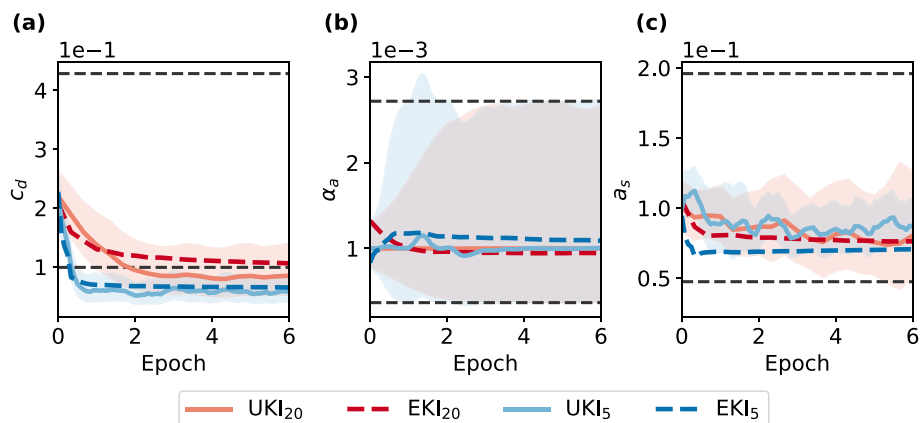


Figure 3. Parameter evolution of the turbulent dissipation (a), updraft advection damping (b), and updraft surface area fraction (c). All values are given in physical space. The lines describe the trajectories of the mean estimate, $\mathcal{T}^{-1}(m_n)$. For unscented Kalman inversion, the marginal $\pm\sigma$ uncertainty band is included in shading. This uncertainty is equal to $\pm\mathcal{T}^{-1}(\sqrt{(\Sigma_n)_{i,i}})$ for the i th parameter. The black dashed lines are the $\pm\sigma$ uncertainty bands of the prior used for regularization. Legend as in Figure 2.

(Figure 2). Subsequent epochs fine-tune the model parameters, further reducing the data-model mismatch. It is remarkable and important that the validation error decreases by about the same magnitude as the training error, demonstrating that the parameterization approach that leverages a physical model generalizes successfully out of the present-climate training sample to a warmer climate.

Both EKI and UKI display efficient training in the low batch-size regime: the validation error tends to be lower for smaller batches after a fixed number of epochs. Hence, decreasing batch size in EKI and UKI can help reduce the computational cost of training models. The optimal batch size will depend on the CPU and wall-clock time constraints of the user. Although using smaller batches reduces CPU time, it requires more serial operations, so using larger batches can reduce wall-clock time.

The sampling noise due to the use of different configurations per batch (e.g., stratocumulus vs. cumulus regimes) increases for smaller batches. Although both algorithms achieve convergence for a wide range of batch sizes, we find that EKI is more robust than UKI to high levels of noise. This is shown in the inset of Figure 2b for $|B| = 5$, and in Appendix D for $|B| = 1$. Other differences between UKI and EKI are observed in Figure 2. The consensus property of EKI leads to a collapse of the model error spread after a few iterations, converging to a point estimate. On the other hand, the UKI ensemble converges to an MSE spread characteristic of the parameter uncertainty as approximated by the distribution $\mathcal{N}(m_n, \Sigma_n)$.

The evolution of the parameter estimate (m_n, Σ_n) is depicted in Figure 3 for the turbulent dissipation c_d , updraft advection damping α_a and surface area fraction a_s . The initial parameter estimate depends on the stochastic initialization for EKI. The UKI estimate provides information about parameter uncertainty, whereas EKI only provides a point estimate (i.e., m_n). From the UKI estimate, we observe that the training set constrains the likely values of the turbulent dissipation (c_d) and surface area fraction (a_s) to a significantly smaller region than the prior. However, the magnitude of updraft advection damping (α_a) is not identifiable using this data set: the corresponding diagonal element of Σ_n converges to the prior variance used in the regularized problem 25 (Figure 3b).

The covariance estimate Σ_n also provides information about correlations between model parameters and total reduction of uncertainty (Figure 4). For the current stratocumulus-to-cumulus transition data set, our EDMF model shows moderate correlations between parameters regulating the turbulence kinetic energy budget in the boundary layer (c_b, c_m, c_d , see Lopez-Gomez et al., 2020). We also find entrainment to be negatively correlated with surface updraft area fraction, detrainment and drag. These correlations can be used to improve parameterizations at the process level by identifying or developing a set of uncorrelated parameters. Figure 4b shows how Σ_n converges to a quasi-steady state estimate of the posterior covariance after ~ 30 iterations.

Vertical profiles of $\bar{q}_l, \overline{w'q'_l}$ and \bar{u} from the validation set are compared to the reference LES profiles in Figure 5. The calibrated model yields smoother and more accurate profiles than the model before training. In particular,

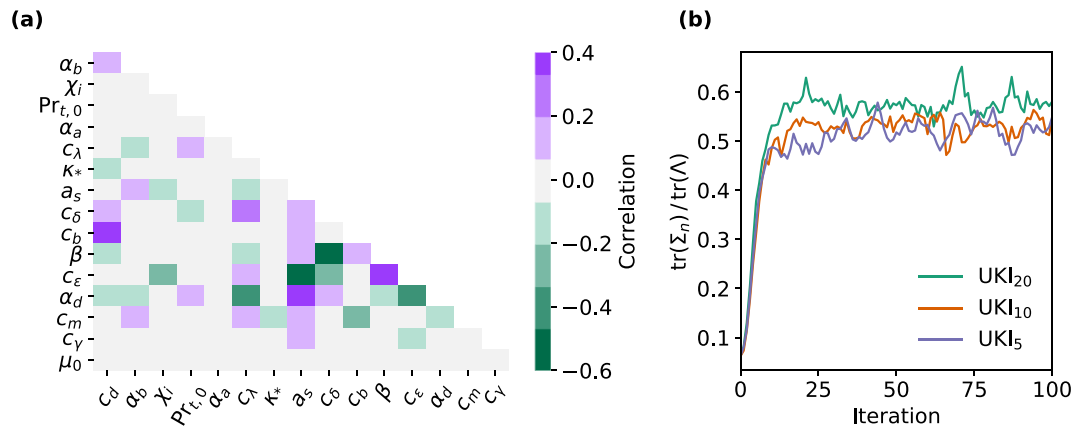


Figure 4. Parameter correlations estimated from unscented Kalman inversion (UKI) using $|B| = 20$ (a), and evolution of the total parameter variance from UKI using $|B| = 20$, 10, and 5, normalized by the prior variance $\text{tr}(\Lambda) = 16$ (b). Note that the initial covariance estimate used in UKI (with $\text{tr}(\Sigma_0) = 1$) is decoupled from the prior. Symbols follow Table 1.

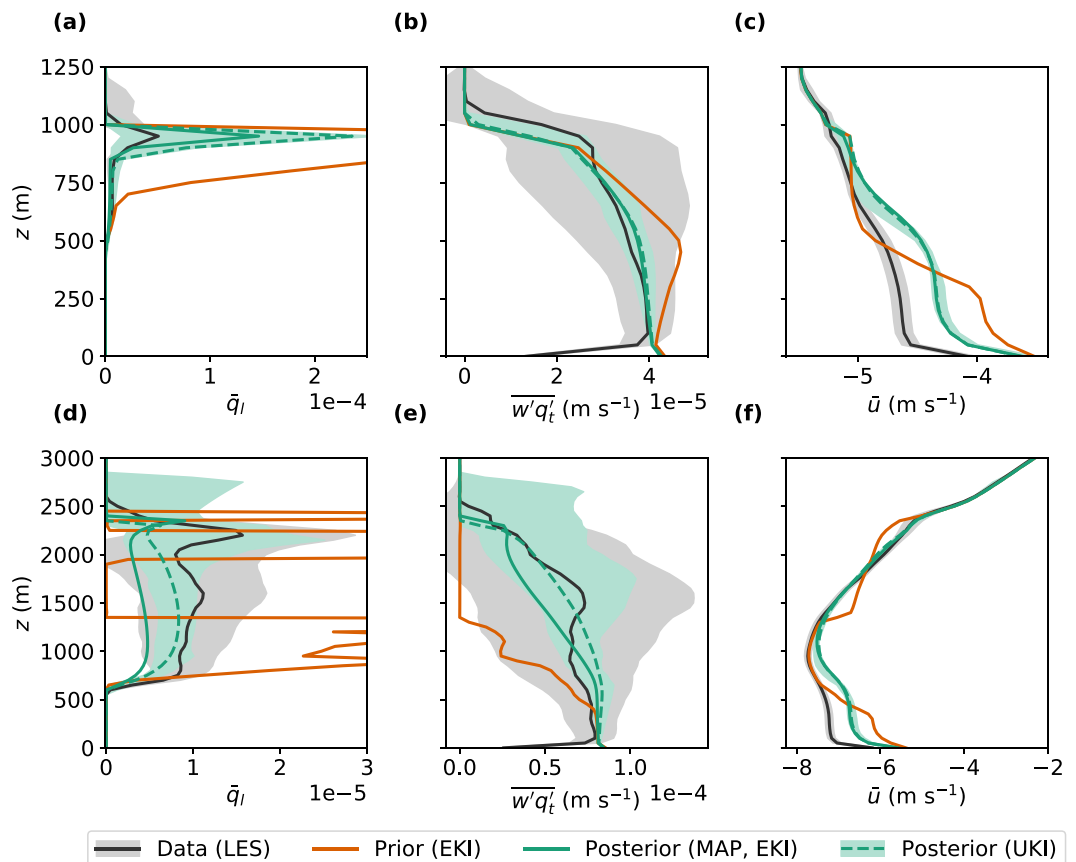


Figure 5. Prior, posterior and large-eddy simulations (LES) profiles of liquid water specific humidity (\bar{q}_l), subgrid-scale moisture flux ($\bar{w}'q'_t$), and zonal velocity (\bar{u}) for cfSites 5 (top) and 14 (the bottom) using July forcing from the AMIP4K experiment as in Shen et al. (2022). The gray shading represents the internal variability of the LES simulations over 6 days of steady forcing, and the lines represent 3-hr time-averaged profiles. Ensemble Kalman inversion prior and posterior results are point estimates evaluated at the parameter vector closest to the ensemble mean. The unscented Kalman inversion posterior shading spans the central 68% of the profile posterior distribution. All Kalman methods used $|B| = 5$ and $J = 2p + 1$.

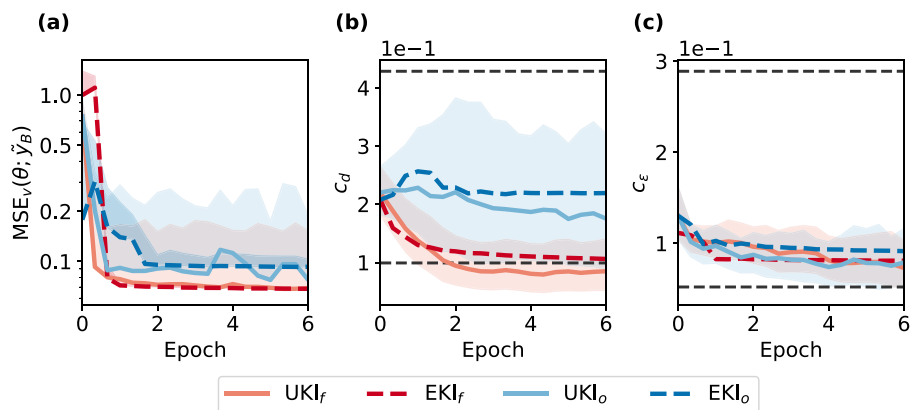


Figure 6. Evolution of the validation error (a), and estimates of the turbulent dissipation (b) and entrainment coefficient (c) for calibration processes using observations of the state 33 at 50 m resolution (UKI_f, EKI_f), or from $\bar{\theta}_l$, \bar{q}_l , and \bar{q}_l at 200 m resolution (UKI_o, EKI_o). All inversion processes use $|B| = 20$. Shading is defined as in Figures 2 and 3.

calibration significantly reduces biases in liquid water specific humidity and moisture transport for both strato-cumulus and cumulus cloud regimes in the 4 K-warmer AMIP4K experiment. These results confirm that the dynamical model can be trained using a low-dimensional encoding of the time statistics, as proposed in Section 2. They also highlight the generalizability of sparse physics-based models.

4.3. Calibration Using Partial Observations

Another application of synthetic high-resolution data is the study of calibration sensitivity to data resolution and partial loss of information. Such sensitivity studies can inform the technical requirements of future observing systems or field campaigns (Suselj et al., 2020), and are easily implemented with ensemble and UKI through modifications of the observational map \mathcal{H} .

Here, we employ the EKI and UKI algorithms for this task by using coarser training data at a vertical resolution of $\Delta z = 200$ m. In addition, we consider only a subset of fields for which observational data may be obtained in practice: the liquid water potential temperature $\bar{\theta}_l$, the total water specific humidity \bar{q}_l , and the liquid water specific humidity \bar{q}_l (National Academies of Sciences, Engineering, and Medicine, 2018; Suselj et al., 2020). Figure 6 compares calibration results using this reduced setup with the results obtained using the full high-resolution observations of Section 4.2. The loss of information is evident in the inability of the algorithms to find the same minimum reached with richer observations. Nevertheless, Kalman inversion significantly reduces the validation error from the prior even with sparser data and a limited number of fields.

The identifiability of individual parameters as a function of the observational map \mathcal{H} can be inferred from the UKI Σ_n diagnostic. Figure 6 shows that the partial observations of temperature and humidity are enough to constrain the entrainment coefficient in the EDMF scheme. However, the loss of information with respect to the original observations leads to much poorer constraints on the turbulent dissipation coefficient. The same comparison can be performed for any parameter of interest to inform observational requirements to constrain models at the process level. This diagnostic is an important advantage of UKI over EKI; identifiability is not directly inferable from EKI due to the ensemble collapse. However, this information can be recovered through the emulation of the forward map (Cleary et al., 2021).

The use of partial observations also highlights the benefits of learning from time statistics instead of tendencies. Learning from statistics not only ensures that the calibrated dynamical model is stable, which requires a leap of faith when training on instantaneous tendencies (Bretherton et al., 2022). It also couples the evolution of thermodynamic and dynamical fields, which can improve the forecast of fields unseen during training. An example is shown in Figure 7. The model calibrated using thermodynamic profiles improves upon the prior model in the forecast of horizontal velocities within the boundary and cloud layers. A common reason to use tendencies for calibration is that they enable the use of supervised learning techniques, which are easy to implement for neural

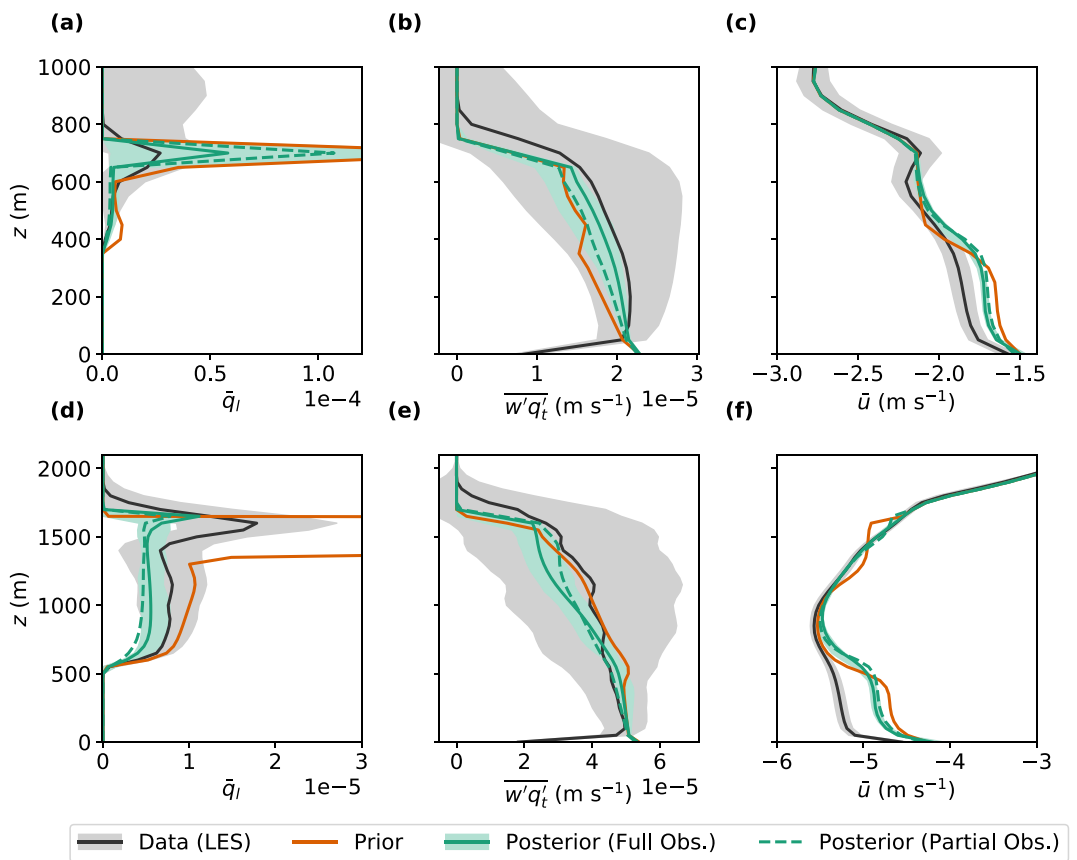


Figure 7. Prior, posterior and large-eddy simulations profiles of liquid water specific humidity (\bar{q}_l), vertical moisture flux ($w'q'_t$), and zonal velocity (\bar{u}) for cfSite 3 using July forcing (the top) and cfSite 14 using January forcing (the bottom) from the AMIP4K experiment (Shen et al., 2022). Posterior results are shown for a model calibrated using the high-resolution state 33 (Full Obs.), and coarse-resolution observations of $\bar{\theta}_l$, \bar{q}_l , and \bar{q}_l (Partial Obs.). Shadings and legend as in Figure 5. Results obtained using unscented Kalman inversion with $|B| = 20$.

network architectures (Bretherton et al., 2022). In the next subsection, we demonstrate the power of UKI and EKI to calibrate hybrid models with embedded neural network parameterizations.

4.4. Calibration of a Hybrid Model With Embedded Neural Network Closures

We consider now a hybrid EDMF scheme that substitutes the dynamical entrainment and detrainment closures proposed by Cohen et al. (2020) with a three-layer dense neural network. We define the fractional entrainment (ϵ) and detrainment (δ) rates as

$$\begin{bmatrix} \epsilon \\ \delta \end{bmatrix} = \frac{1}{z} \text{NN}_3(\Pi_1, \dots, \Pi_6), \quad (35)$$

where z is the height, and the hidden layers of NN_3 have 5 and 4 nodes, from input to outputs. Our closure 35 seeks to learn local expressions for the z -normalized entrainment/detrainment rates, which have been shown to vary weakly in empirical studies of shallow cumulus convection (de Roode et al., 2000; Siebesma, 1996). The neural network inputs Π_1, \dots, Π_6 are 6 nondimensional groups on which entrainment and detrainment may depend, defined as

$$\Pi_1 = \frac{z(b_{up} - b_{en})}{(w_{up} - w_{en})^2 + w_d^2}, \quad (36a)$$

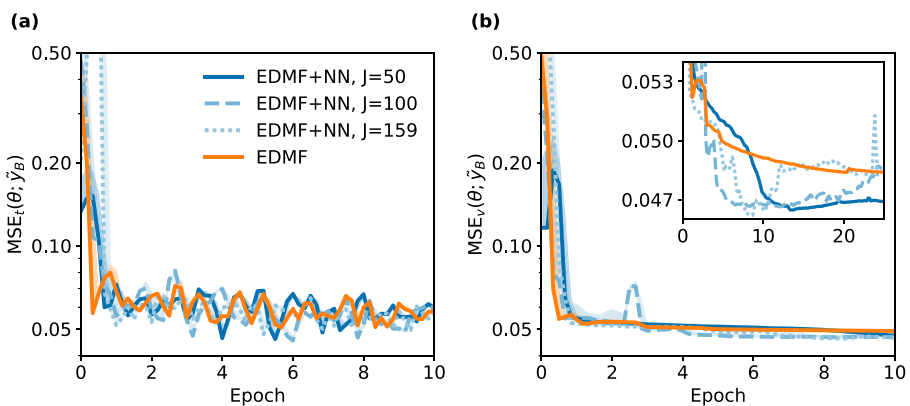


Figure 8. Batch (a) training and (b) validation normalized MSE for the hybrid eddy-diffusivity mass-flux (EDMF + NN) and empirical (EDMF) models. The lines, shading, and inset as in Figure 2. Results are shown for calibration with ensemble Kalman inversion, using $J = 50, 100$ and $2p + 1 = 159$ ensemble members for the hybrid model. The empirical model training uses $J = 2p + 1 = 33$. All inversion processes use batch size $|B| = 10$.

$$\Pi_2 = \frac{a_{up} w_{up}^2 + (1 - a_{up}) w_{en}^2}{2(1 - a_{up}) e_{en} + a_{up} w_{up}^2 + (1 - a_{up}) w_{en}^2}, \quad (36b)$$

$$\Pi_3 = \sqrt{a_{up}}, \quad (36c)$$

$$\Pi_4 = RH_{up} - RH_{en}, \quad (36d)$$

$$\Pi_5 = z/H_{up}, \quad (36e)$$

$$\Pi_6 = gz/R_d T_{ref}. \quad (36f)$$

In Equations 36, $w_d = \left(H_{\text{inv}} \overline{w' b'} \right)_s^{1/3}$ is the Deardorff convective velocity, H_{inv} is the inversion height, $\overline{w' b'}|_s$ is the surface buoyancy flux, g is the gravitational acceleration, R_d is the ideal gas constant for dry air, and T_{ref} is a reference temperature. The subscripts *up* and *en* denote updraft and environment: a_{up} is the updraft area fraction, H_{up} is the updraft top height, and e_{en} is the environmental turbulence kinetic energy. The relative humidity RH, vertical velocity with respect to the grid mean w , and buoyancy b are defined for both updraft and environment.

The neural network closure 35 introduces 63 additional coefficients with respect to the entrainment and detrainment closure calibrated in Sections 4.2 and 4.3, for a total of 79 parameters. As the closure complexity increases, it is most practical to use EKI for calibration, since it enables the use of ensembles with $J < 2p + 1$ members. In Figure 8, we present training and validation errors for the hybrid model using ensemble sizes $J = 50, 100$, and 159, and for the empirical EDMF scheme with $J = 2p + 1 = 33$ ensemble members. We initialize the neural network weights as $\theta_{\text{NN}} \sim \mathcal{N}(\theta_{\text{NN}}^0, I)$ with $\theta_{\text{NN}}^0 \sim U(-0.05, 0.05)$. In all cases, we use Bayesian regularization as discussed in Section 4.2 for all model parameters except for the neural network weights. We calibrate all parameters of the empirical and hybrid models, to compare the optimal performance of both closures.

Both the empirical and hybrid EDMF schemes generalize well to the validation set, with training and validation errors reaching levels of about 5% of the largest a priori validation error. The strong generalization to 4 K-warmer cloud regimes contrasts with results from approaches that try to learn unresolved tendencies directly, without encoding the physics (Rasp et al., 2018). Using a physics-based hybrid approach, all learned closures are consistently placed within the coarse-grained dynamics of the system (Cohen et al., 2020), which also vastly reduces data requirements. Further, targeting closure terms that isolate a single physical process lends itself to interpretability in a manner difficult for purely machine-learning based parameterizations that simultaneously model many physical processes. After training, relationships between EDMF variables and targeted physical quantities like entrainment can be teased out using partial dependence plots or ablation studies. In addition, the learned relationships are point-wise and causal.

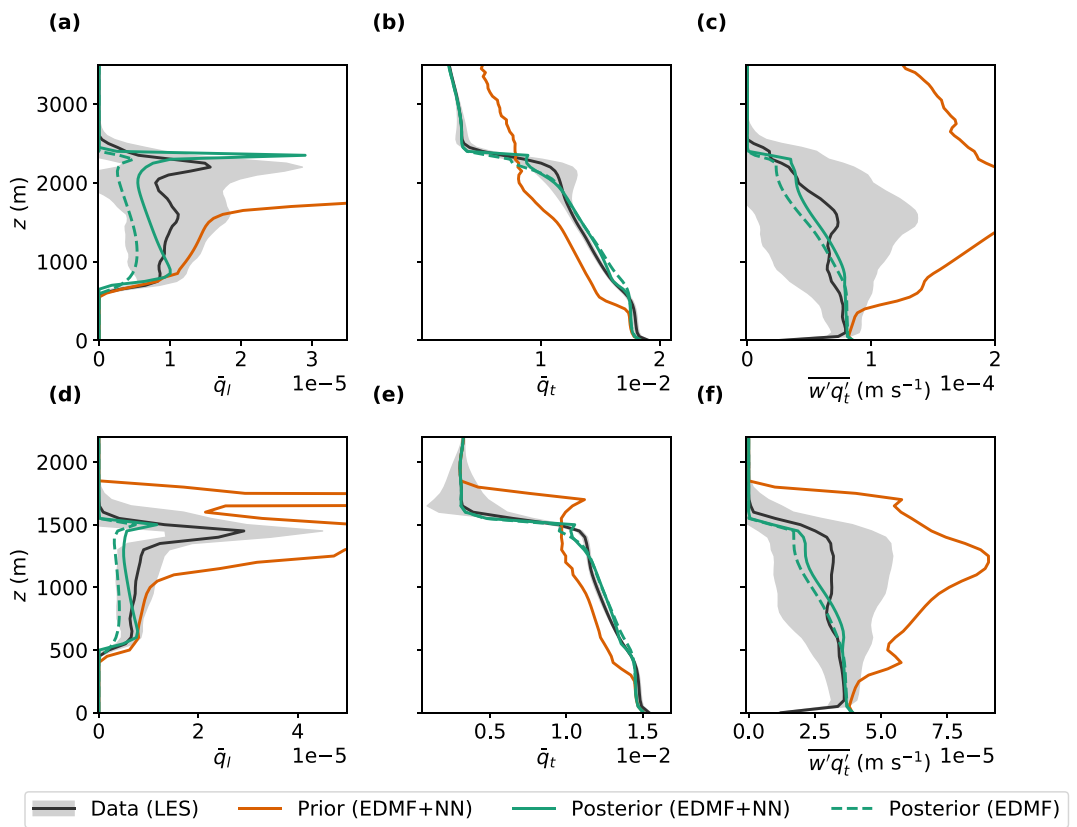


Figure 9. Prior, posterior and large-eddy simulations (LES) profiles of liquid water specific humidity (\bar{q}_l), total water specific humidity (\bar{q}_t), and vertical moisture flux ($\overline{w'q'_t}$) for cfSite 14 using July forcing (top) and cfSite 8 using January forcing (bottom) from the AMIP4K experiment (Shen et al., 2022). Definitions of prior, posterior, and shading as in Figure 5. Posterior results are shown for the eddy-diffusivity mass-flux (EDMF) model with empirical closures (EDMF), and with the neural network entrainment closure 35 (EDMF + NN), using early stopping and 25 epochs of training. Results obtained using ensemble Kalman inversion with $|B| = 10$.

The inset in Figure 8b shows how the higher-complexity hybrid model moderately overfits to the training set after ~ 10 epochs, a behavior that is not observed with the empirical model. Hence, in the low-data regime ($d \lesssim p$), adoption of techniques such as early stopping (Prechelt, 1998) or sparsity-inducing regularization (Schneider et al., 2020) becomes necessary. The compact support property of EKI, which mandates that the solution be in the linear span of the initial ensemble, also regularizes the learned hybrid model with decreasing J ; for $J = 50 < p$ overfitting is significantly reduced. Thus, reducing the ensemble size is an efficient regularization technique when training large machine-learning models that tend to overfit, at the expense of reduced expressivity. Additional EKI-specific regularization techniques for deeper networks are discussed in Kovachki and Stuart (2019).

Another difference between the empirical and the hybrid models is that for the latter, we do not know a priori the parameter ranges for which the model trajectories remain physical. During the training sessions shown in Figure 8, the hybrid models experienced a maximum of 25 ($J = 50$), 30 ($J = 100$), and 72 ($J = 159$) failures in a single iteration, all occurring during the first epoch. The use of the failsafe update proposed in Section 3.1.1 proved crucial to enable training in the presence of model failures, and it reduced the number of failures to a small fraction of the J ensemble members after a few EKI iterations.

Profiles of \bar{q}_l , \bar{q}_t and $\overline{w'q'_t}$ are shown in Figure 9 for the trained empirical and hybrid EDMF models. To produce the profiles with the hybrid model, we retain the parameters learned at the iteration with lowest validation error from a training session spanning 25 epochs, effectively similar to early stopping. As expected from the validation error, the hybrid model slightly improves upon the skill of the empirical model, predicting more accurate profiles of \bar{q}_l within the cloud layer. This is, of course, at the cost of a significantly higher parameter complexity of the closure.

As shown here, EKI allows for rapid prototyping and comparison of closures within an overarching black-box model. Importantly, this comparison can be done during training in terms of the online performance of the fully calibrated dynamical model.

5. Discussion and Conclusions

Ensemble Kalman methods such as ensemble and UKI are powerful tools for training possibly expensive models. By leveraging covariances between the model output and its parameters, they do not impose any constraint on the data used for learning, or the architecture of the closures to be calibrated. This means that ensemble Kalman methods can be used to learn all parameters within complex overarching models, regardless of where those parameters appear in the formulation of the model. Furthermore, the Gaussian approximation of the parameter distribution makes them far more efficient than standard Bayesian inference techniques, at the cost of neglecting uncertainty beyond the second moment of the posterior, and the possible convergence to local minima (as for stochastic gradient descent and other optimization methods).

This enables training physics-based machine-learning parameterizations, as demonstrated here by substituting an internal component of the EDMF model by a neural network, which required no change in the data or framework used for training. The benefits of combining physics and data are demonstrated by the performance of our trained hybrid closure in simulations of clouds typical of conditions 4 K warmer than the clouds in the training set.

To use these algorithms, parameter learning must be framed as an inverse problem. This allows great flexibility, but raises the problem of choosing a reasonable observational map \mathcal{H} and noise covariance Γ to define an inverse problem. Through a domain-agnostic strategy and a reasonable heuristic about the expected model error, we have demonstrated a systematic way of constructing a well-defined inverse problem from high-dimensional data. This strategy is designed to maximize the information content through a lossy principal component encoding \mathcal{H} and to allow the use of time averages as observations, making it amenable to harnessing, for example, satellite observations in addition to computationally generated data. The success of this strategy is demonstrated in a variety of settings, using empirical and hybrid models.

The flexibility of the inverse problem allows to define the observational map \mathcal{H} through any observable diagnostic of the model, be it differentiable or not. For instance, Barthélémy et al. (2021) use a neural network as the mapping \mathcal{H} , to train a low-resolution dynamical model directly from features at high resolution. One could also envision the construction of \mathcal{H} through other statistics of the model dynamics, such as the variance or skewness. These choices may be preferable for particular tasks, such as the prediction of extreme events or the correct representation of emergent phenomena.

Given an inverse problem, we have shown that EKI and UKI are robust to noise and amenable to batching strategies. This establishes the ability of the Kalman algorithms to train models using sequentially sampled data. The same robustness can be expected for other sources of noise, such as stochasticity in the model (Schneider et al., 2021). In addition, we have proposed modifications of the EKI and UKI updates that enable calibrating models that may fail during training, which is often the case for Earth system models.

Although similar, each ensemble Kalman algorithm presents its own relative strengths in our analysis. Calibration through EKI appears to be more robust to noise, and the number of ensemble members may be chosen to be lower than for UKI when the parameter space is high-dimensional. Indeed, Kovachki and Stuart (2019) show successful results for EKI when the number of parameters (e.g., $p \sim 10^6$) is two orders of magnitude higher than the ensemble size. Using fewer ensemble members than parameters also introduces a regularization effect. On the other hand, UKI provides information about parametric uncertainty and correlations, which can be used to improve models at the process level, and to rapidly compare the added value of increasingly precise observing systems. Other ensemble Kalman methods, such as the sparsity-inducing EKI (Schneider et al., 2020) or the ensemble Kalman sampler (Garbuno-Inigo et al., 2020), can provide solutions to the inverse problem with other useful properties. In addition, all these ensemble methods generate parameter-output pairs that can be used to train emulators for uncertainty quantification that can capture non-Gaussian posteriors (Cleary et al., 2021).

Finally, ensemble Kalman methods may be used for the rapid comparison of parameterizations in terms of the online skill of an overarching Earth system model. For example, the same framework could be used to train Gaussian processes, random feature models (Nelsen & Stuart, 2021), Fourier neural operators (Li et al., 2020),

or stochastic closures (Guillaumin & Zanna, 2021). These are some of the exciting research avenues that we will be exploring in the future.

Appendix A: Configuration-Based Principal Component Analysis

Performing PCA on each configuration allows retaining principal modes from low-variance configurations while filtering out trailing modes from high-variance configurations. The importance of this is demonstrated in Figure A1 for three configurations of our LES solver (Pressel et al., 2015) based on observational campaigns of a stable boundary layer, a stratocumulus-topped boundary layer, and shallow cumulus convection (Beare et al., 2006; Siebesma et al., 2003; Stevens et al., 2005). Performing global PCA is equivalent to using a cutoff $\mu_{c,i} > \mu_c^*$ in Figure A1a, where we need to choose between neglecting most modes from certain configurations (e.g., GABLs in Figure A1a) or retaining highly oscillatory modes from others (e.g., Bomex), as measured by the number of zero-crossings of the eigenmode (Hansen, 1998). Highly oscillatory modes may have a disproportionate contribution to the loss when calibrating imperfect models. On the other hand, performing PCA on each $\tilde{\Gamma}_c$ alleviates this problem by aligning the eigenspectra before applying the cutoff, as shown in Figure A1b. Appropriate conditioning of the global covariance matrix is still enforced when applying configuration-based PCA through the Tikhonov regularizer in Equation 14.

Appendix B: Addressing Model Failures With Unscented Kalman Inversion

In the presence of model failures, we perform the UKI quadratures over the successful sigma points. Consider the set of off-center sigma points $\{\hat{\theta}\} = \{\hat{\theta}_s\} \cup \{\hat{\theta}_f\}$ where $\hat{\theta}_s^{(j)}, j = 1, \dots, J_s$ are successful members and $\hat{\theta}_f^{(k)}$ are not. For ease of notation, consider an ordering of $\{\hat{\theta}\}$ such that $\{\hat{\theta}_s\}$ are its first J_s elements, and note that we deal with the central point $\hat{\theta}^{(0)}$ separately. We estimate the covariances $\text{Cov}_q(\mathcal{G}_n, \mathcal{G}_n)$ and $\text{Cov}_q(\theta_n, \mathcal{G}_n)$ from the successful ensemble,

$$\text{Cov}_q(\theta_n, \mathcal{G}_n) \approx \sum_{j=1}^{J_s} w_{s,j} (\hat{\theta}_{s,n}^{(j)} - \bar{\theta}_{s,n}) (\mathcal{G}(\hat{\theta}_{s,n}^{(j)}) - \bar{\mathcal{G}}_{s,n})^T, \quad (\text{B1})$$

$$\text{Cov}_q(\mathcal{G}_n, \mathcal{G}_n) \approx \sum_{j=1}^{J_s} w_{s,j} (\mathcal{G}(\hat{\theta}_{s,n}^{(j)}) - \bar{\mathcal{G}}_{s,n}) (\mathcal{G}(\hat{\theta}_{s,n}^{(j)}) - \bar{\mathcal{G}}_{s,n})^T, \quad (\text{B2})$$

where the weights at each successful sigma point are scaled up, to preserve the sum of weights,

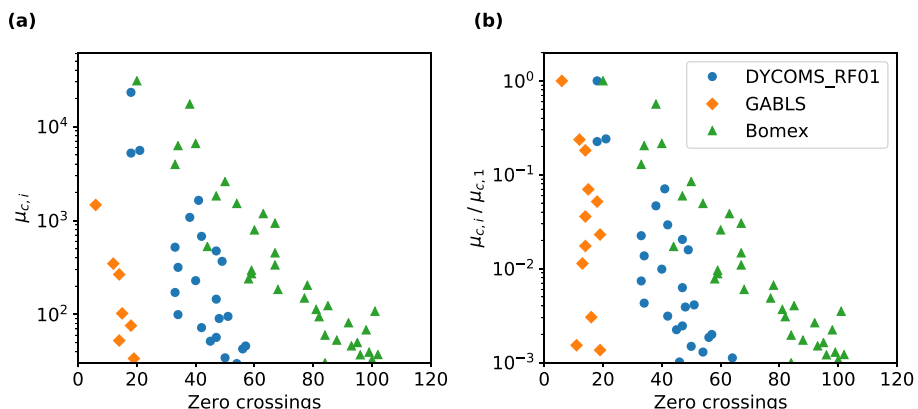


Figure A1. (a) Scatter plot of covariance eigenvalues $\mu_{c,i}$ and the number of zero-crossings of their corresponding eigenmode for three different configurations of a large-eddy simulations solver. (b) The same plot, with eigenvalues normalized by the leading eigenvalue of each configuration ($\mu_{c,1}$). Trailing eigenvalues are associated with high-wavenumber oscillatory modes with frequent sign changes.

$$w_{s,j} = \left(\frac{\sum_{i=1}^{2p} w_i}{\sum_{k=1}^{J_s} w_k} \right) w_j. \quad (B3)$$

In Equations B1 and B2, $\bar{\theta}_{s,n}$ and $\bar{\mathcal{G}}_{s,n}$ must be modified from the original formulation if the central point $\hat{\theta}^{(0)} = m_n$ results in model failure,

$$\bar{\theta}_{s,n} = \begin{cases} m_n & \text{if } \hat{\theta}^{(0)} \text{ successful,} \\ \frac{1}{J_s} \sum_{j=1}^{J_s} \hat{\theta}_{s,n}^{(j)} & \text{otherwise,} \end{cases} \quad (B4)$$

$$\bar{\mathcal{G}}_{s,n} = \begin{cases} \mathcal{G}(m_n) & \text{if } \hat{\theta}^{(0)} \text{ successful,} \\ \frac{1}{J_s} \sum_{j=1}^{J_s} \mathcal{G}(\hat{\theta}_{s,n}^{(j)}) & \text{otherwise.} \end{cases} \quad (B5)$$

These modified UKI quadrature rules are used throughout Section 4 to deal with model failures. Since UKI can be initialized from a tighter prior than EKI, due to the absence of ensemble collapse, failures are much easier to avoid than with EKI.

Appendix C: Parameter Transformation and Prior

Given a prior range $[\phi_i, \phi_f]$ for a parameter $\phi \in \mathbb{R}$, we define the transformation

$$\theta = \mathcal{T}(\phi) = \ln \frac{\phi - \phi_i}{\phi_f - \phi}, \quad (C1)$$

such that the interval midpoint is mapped to $\theta = 0$, and the bounds to $\pm\infty$. An unconstrained Gaussian prior may then be defined for θ , given the prior mean in physical (constrained) parameter space ϕ_p as

$$\theta_0 \sim \mathcal{N}(\mathcal{T}(\phi_p), \sigma_0^2), \quad (C2)$$

where σ_0^2 is a free parameter controlling the size of the region within the interval $[\phi_i, \phi_f]$ containing most of the probability. This means that the magnitude of σ_0 is already normalized with respect to the prior range, so we will generally choose $\sigma_0 \sim \mathcal{O}(1)$. The p -dimensional prior $\mathcal{N}(m_0, \Sigma_0)$ is then constructed as an uncorrelated multivariate normal with marginal distributions given by Equation C2. The normalization induced by Equation C1 also enables the use of isotropic regularization in Equations 25 and 26, even though the physical parameters ϕ may differ in order of magnitude. For more examples of parameter transformations in the context of EKI and UKI, see Huang, Schneider, and Stuart (2022), Schneider et al. (2022), and Dunbar et al. (2022).

Appendix D: Calibration Using Very Noisy Loss Evaluations

The Kalman inversion results are expected to deteriorate above some noise threshold, as the signal-to-noise ratio in the training process decreases. We explored the sensitivity of UKI and EKI to noise by sampling a single configuration per iteration from the training set described in Section 4.1. As shown in Figure D1, UKI fails to converge to the minimum found with larger batches in this limit. The validation error is characterized by large oscillations due to strong changes in the value of model parameters like the entrainment coefficient c_e or the eddy viscosity coefficient c_m . On the other hand, EKI proves robust to noise even in this limit, converging to the minimum found by UKI employing larger batches.

In the context of Kalman inversion, decreasing the step size Δt is equivalent to increasing the noise variance, as shown in Equations 18 and 27. We investigate the time step role in the small batch limit by performing the EKI with $\Delta t = |C|^{-1} = 1/60$. The smaller time step increases the parameter uncertainty, which leads to a reduction in parameter oscillations and estimates closer to the prior. This is accompanied by a moderate reduction in validation error oscillations. We performed additional inversions using even smaller time steps, which resulted in a convergence of the parameter estimates toward the prior and a minor reduction in validation error with respect to

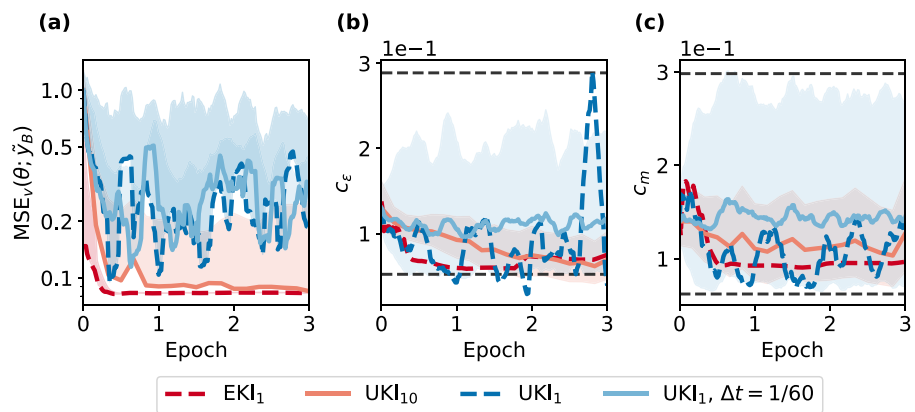


Figure D1. Evolution of the validation error (a) and estimates of the entrainment (b), and eddy diffusivity (c) coefficients. Results shown for unscented Kalman inversion (UKI) using batch sizes of 10 and 1, and ensemble Kalman inversion using a batch size of 1. Parameter uncertainty only shown for UKI₁₀ and UKI₁, $\Delta t = 1/60$ for clarity. All results shown use $\Delta t = |C|/|B|$ unless otherwise specified. Shading as in Figures 2 and 3.

the initialization. We conclude that decreasing Δt in UKI can reduce oscillations due to high levels of noise, but it does not result in the same robustness as EKI.

Notation

$\phi \in \mathbb{R}^p$	learnable parameters, in physical space
$\theta \in \mathbb{R}^p$	transformed learnable parameters, in unconstrained space
$\theta^* \in \mathbb{R}^p$	optimal unconstrained parameter estimate (MAP or MLE)
φ_0	initial dynamical state
F_φ	dynamical forcing
$x_c = \{\varphi_0, F_\varphi\}_c$	configuration of the dynamical system
$\zeta(x_c) : \varphi_0 \rightarrow \varphi(t)$	true dynamical system evolution
$\Psi(\phi; x_c) : \varphi_0 \rightarrow \hat{\varphi}(t)$	dynamical model evolution
\mathcal{H}_c	observational map for configuration c
$y_c \in \mathbb{R}^{d_c}$	observation vector for configuration c
$\eta_c \in \mathbb{R}^{d_c}$	observation error for map \mathcal{H}_c
$\delta(x_c) \in \mathbb{R}^{d_c}$	model or representation error for configuration c
$\Gamma_c \in \mathbb{R}^{d_c \times d_c}$	covariance of the Gaussian noise $\eta_c + \delta(x_c)$
$\mathcal{G}_c : \mathbb{R}^p \rightarrow \mathbb{R}^{d_c}$	forward model for configuration c
$C = \{x_c, c = 1, \dots, C \}$	set of configurations
$y = [y_1, \dots, y_{ C }]^T \in \mathbb{R}^d$	global observation vector
$\delta = [\delta(x_1), \dots, \delta(x_{ C })]^T$	global representation error
$\eta = [\eta_1, \dots, \eta_{ C }]^T$	global observation error
$\Gamma \in \mathbb{R}^{d \times d}$	global noise covariance matrix
$\mathcal{T} : U \rightarrow \mathbb{R}^p$	parameter transformation to unconstrained space
$\mathcal{G} : \mathbb{R}^p \rightarrow \mathbb{R}^d$	forward model
$\rho(\theta y, \Gamma)$	parameter posterior probability density, given Γ and y
$\rho_{\text{prior}}(\theta)$	parameter prior probability density, independent of Γ
$\mathcal{L} : \mathbb{R}^p \times \mathbb{R}^d \rightarrow \mathbb{R}$	loss or negative log-likelihood given Γ
$S_c(t) \in \mathbb{R}^{\tilde{d}_c}$	observed state
$V_{c,j}(t) \in \mathbb{R}^{h_c}$	spatial field j within the observed state S_c
$s_c(t) \in \mathbb{R}^{\tilde{d}_c}$	normalized observed state
$v_{c,j}(t) \in \mathbb{R}^{h_c}$	spatial field j within the normalized state s_c

$\sigma_{c,j} \in \mathbb{R}$	pooled time standard deviation of $V_{c,j}$
$T_c \in \mathbb{R}$	time-averaging window used in map \mathcal{H}_c
$\tilde{y}_c \in \mathbb{R}^{\tilde{d}_c}$	counterpart of y_c prior to encoding
$\tilde{y} \in \mathbb{R}^{\tilde{d}}$	global observation vector prior to encoding
$\tilde{\Gamma}_c \in \mathbb{R}^{\tilde{d}_c \times \tilde{d}_c}$	counterpart of Γ_c prior to encoding
$\tilde{\Gamma} \in \mathbb{R}^{\tilde{d} \times \tilde{d}}$	counterpart of Γ prior to encoding
$I_d \in \mathbb{R}^{d \times d}$	identity matrix of size $d \times d$
$\mu_{c,i} \in \mathbb{R}$	i th largest eigenvalue of $\tilde{\Gamma}_c$
$\kappa \in \mathbb{R}$	approximate condition number of a matrix
$r_c \in \mathbb{R}$	approximate rank of matrix $\tilde{\Gamma}_c$
$\epsilon_m \in \mathbb{R}$	machine or data precision
$\kappa_* < \epsilon_m^{-1/2}$	limiting matrix condition number
$P_c \in \mathbb{R}^{\tilde{d}_c \times d_c}$	truncated PCA projection matrix
$D\mathcal{G}(\theta) \in \mathbb{R}^{d \times p}$	Jacobian of forward model at θ
$B = \{x_c, c = 1, \dots, B \}$	mini-batch of configurations
$L : \mathbb{R}^p \times \mathbb{R}^d \rightarrow \mathbb{R}$	configuration-averaged loss
$y_B \in \mathbb{R}^{d_B}$	observation vector for batch B
$\tilde{y}_B \in \mathbb{R}^{\tilde{d}_B}$	counterpart of y_B prior to encoding
$\tilde{\mathcal{G}}_B : \mathbb{R}^p \rightarrow \mathbb{R}^{\tilde{d}_B}$	forward model corresponding to observations \tilde{y}_B
$\Theta_n \in \mathbb{R}^{p \times J}$	parameter ensemble at iteration n
$m_n \in \mathbb{R}^p$	mean parameter estimate at iteration n
$\Sigma_n \in \mathbb{R}^{p \times p}$	parameter covariance estimate at iteration n
$\mathcal{G}_{\Theta_n} \in \mathbb{R}^{d \times J}$	forward model evaluation ensemble at iteration n
$\varepsilon(\Theta_n) \in \mathbb{R}^{d \times J}$	data-model mismatch ensemble at iteration n
$\Delta t \in \mathbb{R}$	nominal learning rate
$\Theta_{s,n} \in \mathbb{R}^{p \times J_s}$	successful parameter ensemble at iteration n
$\theta_{f,n}^{(k)} \in \mathbb{R}^p$	k th failed parameter vector at iteration n
$m_p \in \mathbb{R}^p$	parameter prior mean
$\Lambda \in \mathbb{R}^{p \times p}$	gaussian prior covariance
$y_a \in \mathbb{R}^{d+p}$	observation vector augmented with m_p
$\mathcal{G}_a(\theta) \in \mathbb{R}^{d+p}$	forward model augmented with θ
$\xi \in \mathbb{R}^{d+p}$	aggregate noise in the augmented data-model relation
$\Gamma_a \in \mathbb{R}^{(d+p) \times (d+p)}$	covariance of the aggregate noise ξ
$\hat{\Pi}_j^{(j)} \in \mathbb{R}^p$	j th sigma point for UKI quadrature
Π_j	j th nondimensional input to neural network

Acknowledgments

We thank Daniel Z. Huang and Zhaoyi Shen for insightful discussions, and Julien Brajard and an anonymous reviewer for prompting a clearer and more precise formulation of the problem and methods discussed in this study. I. L. was supported by a fellowship from the Resnick Sustainability Institute at Caltech, and an Amazon AI4Science fellowship. H. L. L. E. was supported by an Aker scholar and a Fulbright fellowship. This research was additionally supported by the generosity of Eric and Wendy Schmidt by recommendation of the Schmidt Futures program, by the National Science Foundation (Grant No. AGS-1835860), by the Defense Advanced Research Projects Agency (Agreement No. HR00112290030), and by the Heising-Simons Foundation. Part of this research was carried out at the Jet Propulsion Laboratory, California Institute of Technology, under a contract with the National Aeronautics and Space Administration.

Data Availability Statement

The software package implementing ensemble Kalman methods can be accessed at <https://doi.org/10.5281/zenodo.6382968>, the one implementing the eddy-diffusivity mass-flux (EDMF) scheme at <https://doi.org/10.5281/zenodo.6392397>, and the software used to calibrate the EDMF scheme may be accessed at <https://doi.org/10.5281/zenodo.6382865>. The data from Shen et al. (2022) used for model training are available at <https://doi.org/10.22002/D1.20052>.

References

Anderson, J. L. (2012). Localization and sampling error correction in ensemble Kalman filter data assimilation. *Monthly Weather Review*, 140(7), 2359–2371. <https://doi.org/10.1175/MWR-D-11-00013.1>

Anderson, J. L., & Anderson, S. L. (1999). A Monte Carlo implementation of the nonlinear filtering problem to produce ensemble assimilations and forecasts. *Monthly Weather Review*, 127(12), 2741–2758. [https://doi.org/10.1175/1520-0493\(1999\)127<2741:AMCIOT>2.0.CO;2](https://doi.org/10.1175/1520-0493(1999)127<2741:AMCIOT>2.0.CO;2)

Barthélémy, S., Brajard, J., Bertino, L., & Counillon, F. (2021). Super-resolution data assimilation. <https://doi.org/10.48550/arxiv.2109.08017>

Beare, R. J., Macvean, M. K., Holtslag, A. A. M., Cuxart, J., Esau, I., Golaz, J.-C., et al. (2006). An intercomparison of large-eddy simulations of the stable boundary layer. *Boundary-Layer Meteorology*, 118(2), 247–272. <https://doi.org/10.1007/s10546-004-2820-6>

Beucler, T., Pritchard, M., Rasp, S., Ott, J., Baldi, P., & Gentine, P. (2021). Enforcing analytic constraints in neural networks emulating physical systems. *Physical Review Letters*, 126(9), 98302. <https://doi.org/10.1103/PhysRevLett.126.098302>

Bocquet, M., & Sakov, P. (2013). Joint state and parameter estimation with an iterative ensemble Kalman smoother. *Nonlinear Processes in Geophysics*, 20(5), 803–818. <https://doi.org/10.5194/npg-20-803-2013>

Brajard, J., Carrassi, A., Bocquet, M., & Bertino, L. (2021). Combining data assimilation and machine learning to infer unresolved scale parametrization. *Philosophical Transactions of the Royal Society A: Mathematical, Physical & Engineering Sciences*, 379(2194), 20200086. <https://doi.org/10.1098/rsta.2020.0086>

Brenowitz, N. D., Beucler, T., Pritchard, M., & Bretherton, C. S. (2020). Interpreting and stabilizing machine-learning parametrizations of convection. *Journal of the Atmospheric Sciences*, 77(12), 4357–4375. <https://doi.org/10.1175/JAS-D-20-0082.1>

Brenowitz, N. D., & Bretherton, C. S. (2018). Prognostic validation of a neural network unified physics parameterization. *Geophysical Research Letters*, 45(12), 6289–6298. <https://doi.org/10.1029/2018GL078510>

Bretherton, C. S., Henn, B., Kwa, A., Brenowitz, N. D., Watt-Meyer, O., McGibbon, J., et al. (2022). Correcting coarse-grid weather and climate models by machine learning from global storm-resolving simulations. *Journal of Advances in Modeling Earth Systems*, 14(2), e2021MS002794. <https://doi.org/10.1029/2021MS002794>

Brynjarsdóttir, J., & O'Hagan, A. (2014). Learning about physical parameters: The importance of model discrepancy. *Inverse Problems*, 30(11), 114007. <https://doi.org/10.1088/0266-5611/30/11/114007>

Burgers, G., van Leeuwen, P. J., & Evensen, G. (1998). Analysis scheme in the ensemble Kalman filter. *Monthly Weather Review*, 126(6), 1719–1724. [https://doi.org/10.1175/1520-0493\(1998\)126<1719:ASITEK>2.0.CO;2](https://doi.org/10.1175/1520-0493(1998)126<1719:ASITEK>2.0.CO;2)

Chada, N. K., Stuart, A. M., & Tong, X. T. (2020). Tikhonov regularization within ensemble Kalman inversion. *SIAM Journal on Numerical Analysis*, 58, 1263–1294. <https://doi.org/10.1137/19M1242331>

Chen, Y., & Oliver, D. S. (2012). Ensemble randomized maximum likelihood method as an iterative ensemble smoother. *Mathematical Geosciences*, 44, 1–26. <https://doi.org/10.1007/s11004-011-9376-z>

Cleary, E., Garbuno-Íñigo, A., Lan, S., Schneider, T., & Stuart, A. M. (2021). Calibrate, emulate, sample. *Journal of Computational Physics*, 424, 109716. <https://doi.org/10.1016/j.jcp.2020.109716>

Cohen, Y., Lopez-Gomez, I., Jaruga, A., He, J., Kaul, C. M., & Schneider, T. (2020). Unified entrainment and detrainment closures for extended eddy-diffusivity mass-flux schemes. *Journal of Advances in Modeling Earth Systems*, 12(9), e2020MS002162. <https://doi.org/10.1029/2020MS002162>

Cohn, S. E. (1997). An introduction to estimation theory. *Journal of the Meteorological Society of Japan. Ser. II*, 75(1B), 257–288. https://doi.org/10.2151/jmsj1965.75.1B_257

Cotter, S. L., Roberts, G. O., Stuart, A. M., & White, D. (2013). MCMC methods for functions: Modifying old algorithms to make them faster. *Statistical Science*, 28(3), 424–446. <https://doi.org/10.1214/13-STS421>

de Roode, S. R., Duynderke, P. G., & Siebesma, A. P. (2000). Analogies between mass-flux and Reynolds-averaged equations. *Journal of the Atmospheric Sciences*, 57(10), 1585–1598. [https://doi.org/10.1175/1520-0469\(2000\)057<1585:ABMFAR>2.0.CO;2](https://doi.org/10.1175/1520-0469(2000)057<1585:ABMFAR>2.0.CO;2)

Dunbar, O., Howland, M. F., Schneider, T., & Stuart, A. (2022). Ensemble-based experimental design for targeted high-resolution simulations to inform climate models. *Earth and Space Science Open Archive*, 24. <https://doi.org/10.1002/essoar.10510142.1>

Emerick, A. A., & Reynolds, A. C. (2013). Ensemble smoother with multiple data assimilation. *Computers & Geosciences*, 55, 3–15. <https://doi.org/10.1016/j.cageo.2012.03.011>

Evensen, G. (1994). Sequential data assimilation with a nonlinear quasi-geostrophic model using Monte Carlo methods to forecast error statistics. *Journal of Geophysical Research*, 99(C5), 10143–10162. <https://doi.org/10.1029/94JC00572>

Garbuno-Íñigo, A., Hoffmann, F., Li, W., & Stuart, A. M. (2020). Interacting Langevin diffusions: Gradient structure and ensemble Kalman sampler. *SIAM Journal on Applied Dynamical Systems*, 19(1), 412–441. <https://doi.org/10.1137/19M1251655>

Guillaumin, A. P., & Zanna, L. (2021). Stochastic-deep learning parameterization of ocean momentum forcing. *Journal of Advances in Modeling Earth Systems*, 13(9), e2021MS002534. <https://doi.org/10.1029/2021MS002534>

Hansen, P. C. (1990). Truncated singular value decomposition solutions to discrete ill-posed problems with ill-determined numerical rank. *SIAM Journal on Scientific and Statistical Computing*, 11(3), 503–518. <https://doi.org/10.1137/0911028>

Hansen, P. C. (1998). Rank-deficient and discrete ill-posed problems. *Society for Industrial and Applied Mathematics*. <https://doi.org/10.1137/1.9780898719697>

He, J., Cohen, Y., Lopez-Gomez, I., Jaruga, A., & Schneider, T. (2021). An improved perturbation pressure closure for eddy-diffusivity mass-flux schemes. *Earth and Space Science Open Archive*, 37. <https://doi.org/10.1002/essoar.10505084.2>

Houtekamer, P. L., & Mitchell, H. L. (1998). Data assimilation using an ensemble Kalman filter technique. *Monthly Weather Review*, 126(3), 796–811. [https://doi.org/10.1175/1520-0493\(1998\)126<0796:DAUAEK>2.0.CO;2](https://doi.org/10.1175/1520-0493(1998)126<0796:DAUAEK>2.0.CO;2)

Houtekamer, P. L., & Mitchell, H. L. (2001). A sequential ensemble Kalman filter for atmospheric data assimilation. *Monthly Weather Review*, 129(1), 123–137. [https://doi.org/10.1175/1520-0493\(2001\)129<0123:ASEKFF>2.0.CO;2](https://doi.org/10.1175/1520-0493(2001)129<0123:ASEKFF>2.0.CO;2)

Huang, D. Z., Huang, J., Reich, S., & Stuart, A. M. (2022). Efficient derivative-free Bayesian inference for large-scale inverse problems. <https://doi.org/10.48550/arxiv.2204.04386>

Huang, D. Z., Schneider, T., & Stuart, A. M. (2022). Iterated Kalman methodology for inverse problems. *Journal of Computational Physics*, 463, 111262. <https://doi.org/10.1016/j.jcp.2022.111262>

Iglesias, M. A. (2016). A regularizing iterative ensemble Kalman method for PDE-constrained inverse problems. *Inverse Problems*, 32(2), 025002. <https://doi.org/10.1088/0266-5611/32/2/025002>

Iglesias, M. A., Law, K. J. H., & Stuart, A. M. (2013). Ensemble Kalman methods for inverse problems. *Inverse Problems*, 29(4), 045001. <https://doi.org/10.1088/0266-5611/29/4/045001>

Kaipio, J., & Somersalo, E. (2006). *Statistical and computational inverse problems* (Vol. 160). Springer Science & Business Media.

Kennedy, M., & O'Hagan, A. (2001). Bayesian calibration of computer models. *Journal of the Royal Statistical Society: Series B*, 63(3), 425–464. <https://doi.org/10.1111/1467-9868.00294>

Keskar, N. S., Mudigere, D., Nocedal, J., Smelyanskiy, M., & Tang, P. T. P. (2016). On large-batch training for deep learning: Generalization gap and sharp minima. <https://doi.org/10.48550/arXiv.1609.04836>

Kovachki, N. B., & Stuart, A. M. (2019). Ensemble Kalman inversion: A derivative-free technique for machine learning tasks. *Inverse Problems*, 35(9), 095005. <https://doi.org/10.1088/1361-6420/ab1c3a>

Lee, Y. (2021). Sampling error correction in ensemble Kalman inversion. <https://doi.org/10.48550/arxiv.2105.11341>

Li, M., Zhang, T., Chen, Y., & Smola, A. J. (2014). Efficient mini-batch training for stochastic optimization. *ACM*. <https://doi.org/10.1145/262330.2623612>

Li, Z., Kovachki, N., Azizzadenesheli, K., Liu, B., Bhattacharya, K., Stuart, A., & Anandkumar, A. (2020). Fourier neural operator for parametric partial differential equations. <https://doi.org/10.48550/arxiv.2010.08895>

Ling, J., Kurzawski, A., & Templeton, J. (2016). Reynolds averaged turbulence modelling using deep neural networks with embedded invariance. *Journal of Fluid Mechanics*, 807, 155–166. <https://doi.org/10.1017/jfm.2016.615>

Lopez-Gomez, I., Cohen, Y., He, J., Jaruga, A., & Schneider, T. (2020). A generalized mixing length closure for eddy-diffusivity mass-flux schemes of turbulence and convection. *Journal of Advances in Modeling Earth Systems*, 12(11), e2020MS002161. <https://doi.org/10.1029/2020MS002161>

Lopez-Gomez, I., McGovern, A., Agrawal, S., & Hickey, J. (2022). Global extreme heat forecasting using neural weather models. <https://doi.org/10.48550/arxiv.2205.10972>

Lorenz, E. N. (1975). Climatic predictability. In *The physical basis of climate and climate modelling* (Vol. 16, pp. 132–136). World Meteorological Organization.

Metropolis, N., Rosenbluth, A. W., Rosenbluth, M. N., Teller, A. H., & Teller, E. (1953). Equation of state calculations by fast computing machines. *The Journal of Chemical Physics*, 21(6), 1087–1092. <https://doi.org/10.1063/1.1699114>

Meyer, D., Hogan, R. J., Dueben, P. D., & Mason, S. L. (2022). Machine learning emulation of 3D cloud radiative effects. *Journal of Advances in Modeling Earth Systems*, 14(3), e2021MS002550. <https://doi.org/10.1029/2021MS002550>

Mlawer, E. J., Taubman, S. J., Brown, P. D., Iacono, M. J., & Clough, S. A. (1997). Radiative transfer for inhomogeneous atmospheres: RRTM, a validated correlated-k model for the longwave. *Journal of Geophysical Research*, 102(D14), 16663–16682. <https://doi.org/10.1029/97JD00237>

Moral, P. D., Doucet, A., & Jasra, A. (2006). Sequential Monte Carlo samplers. *Journal of the Royal Statistical Society: Series B*, 68(3), 411–436. <https://doi.org/10.1111/j.1467-9868.2006.00553.x>

Morozfeld, M., Adams, J., Lunderman, S., & Orozco, R. (2018). Feature-based data assimilation in geophysics. *Nonlinear Processes in Geophysics*, 25(2), 355–374. <https://doi.org/10.5194/npg-25-355-2018>

Muñoz-Sabater, J., Dutra, E., Agustí-Panareda, A., Albergel, C., Arduini, G., Balsamo, G., et al. (2021). ERA5-Land: A state-of-the-art global reanalysis dataset for land applications. *Earth System Science Data*, 13(9), 4349–4383. <https://doi.org/10.5194/essd-13-4349-2021>

National Academies of Sciences, Engineering, and Medicine. (2018). *Thriving on our changing planet: A decadal strategy for Earth observation from space*. The National Academies Press. <https://doi.org/10.17226/24938>

Nelsen, N. H., & Stuart, A. M. (2021). The random feature model for input-output maps between Banach spaces. *SIAM Journal on Scientific Computing*, 43(5), A3212–A3243. <https://doi.org/10.1137/20M133957X>

Pathak, J., Subramanian, S., Harrington, P., Raja, S., Chattopadhyay, A., Mardani, M., et al. (2022). FourCastNet: A global data-driven high-resolution weather model using adaptive Fourier neural operators. <https://doi.org/10.48550/arxiv.2202.11214>

Prechelt, L. (1998). *Early stopping—but when?* Springer Berlin Heidelberg. https://doi.org/10.1007/3-540-49430-8_3

Pressel, K. G., Kaul, C. M., Schneider, T., Tan, Z., & Mishra, S. (2015). Large-eddy simulation in an anelastic framework with closed water and entropy balances. *Journal of Advances in Modeling Earth Systems*, 7(3), 1425–1456. <https://doi.org/10.1002/2015MS000496>

Rasp, S., Pritchard, M. S., & Gentine, P. (2018). Deep learning to represent subgrid processes in climate models. *Proceedings of the National Academy of Sciences*, 115(39), 9684–9689. <https://doi.org/10.1073/pnas.1810286115>

Rasp, S., & Thuerey, N. (2021). Data-driven medium-range weather prediction with a Resnet pretrained on climate simulations: A new model for WeatherBench. *Journal of Advances in Modeling Earth Systems*, 13(2), e2020MS002405. <https://doi.org/10.1029/2020MS002405>

Ravuri, S., Lenc, K., Willson, M., Kangin, D., Lam, R., Mirowski, P., et al. (2021). Skilful precipitation nowcasting using deep generative models of radar. *Nature*, 597(7787), 672–677. <https://doi.org/10.1038/s41586-021-03854-z>

Reichel, L., & Rodriguez, G. (2013). Old and new parameter choice rules for discrete ill-posed problems. *Numerical Algorithms*, 63(1), 65–87. <https://doi.org/10.1007/s11075-012-9612-8>

Reichstein, M., Camps-Valls, G., Stevens, B., Jung, M., Denzler, J., Carvalhais, N., & Prabhat (2019). Deep learning and process understanding for data-driven Earth system science. *Nature*, 566(7743), 195–204. <https://doi.org/10.1038/s41586-019-0912-1>

Schillings, C., & Stuart, A. M. (2017). Analysis of the ensemble Kalman filter for inverse problems. *SIAM Journal on Numerical Analysis*, 55(3), 1264–1290. <https://doi.org/10.1137/16M105959X>

Schmit, T. J., Griffith, P., Gunshor, M. M., Daniels, J. M., Goodman, S. J., & Lebair, W. J. (2017). A closer look at the ABI on the GOES-R series. *Bulletin of the American Meteorological Society*, 98(4), 681–698. <https://doi.org/10.1175/BAMS-D-15-00230.1>

Schneider, T., Dunbar, O. R. A., Wu, J., Böttcher, L., Burov, D., Garbuno-Iturgo, A., et al. (2022). Epidemic management and control through risk-dependent individual contact interventions. *PLOS Computational Biology*, 18(6). <https://doi.org/10.1371/journal.pcbi.1010171>

Schneider, T., & Griffies, S. M. (1999). A conceptual framework for predictability studies. *Journal of Climate*, 12(10), 3133–3155. [https://doi.org/10.1175/1520-0442\(1999\)012<3133:ACFFPS>2.0.CO;2](https://doi.org/10.1175/1520-0442(1999)012<3133:ACFFPS>2.0.CO;2)

Schneider, T., Lan, S., Stuart, A., & Teixeira, J. (2017). Earth system modeling 2.0: A blueprint for models that learn from observations and targeted high-resolution simulations. *Geophysical Research Letters*, 44(24), 312–396. <https://doi.org/10.1002/2017GL076101>

Schneider, T., Stuart, A. M., & Wu, J.-L. (2020). Ensemble Kalman inversion for sparse learning of dynamical systems from time-averaged data. <https://doi.org/10.48550/arxiv.2007.06175>

Schneider, T., Stuart, A. M., & Wu, J.-L. (2021). Learning stochastic closures using ensemble Kalman inversion. *Transactions of Mathematics and Its Applications*, 5(1), tnab003. <https://doi.org/10.1093/imatrtnab003>

Seifert, A., & Rasp, S. (2020). Potential and limitations of machine learning for modeling warm-rain cloud microphysical processes. *Journal of Advances in Modeling Earth Systems*, 12, e2020MS002301. <https://doi.org/10.1029/2020MS002301>

Shen, Z., Sridhar, A., Tan, Z., Jaruga, A., & Schneider, T. (2022). A library of large-eddy simulations forced by global climate models. *Journal of Advances in Modeling Earth Systems*, 14(3), e2021MS002631. <https://doi.org/10.1029/2021MS002631>

Siebesma, A. P. (1996). On the mass flux approach for atmospheric convection. In *Workshop on new insights and approaches to convective parameterization* (pp. 25–57). ECMWF.

Siebesma, A. P., Bretherton, C. S., Brown, A., Chlond, A., Cuxart, J., Duynkerke, P. G., et al. (2003). A large eddy simulation intercomparison study of shallow cumulus convection. *Journal of the Atmospheric Sciences*, 60(10), 1201–1219. [https://doi.org/10.1175/1520-0469\(2003\)60<1201:ALESIS>2.0.CO;2](https://doi.org/10.1175/1520-0469(2003)60<1201:ALESIS>2.0.CO;2)

Sønderby, C. K., Espeholt, L., Heek, J., Dehghani, M., Oliver, A., Salimans, T., et al. (2020). MetNet: A neural weather model for precipitation forecasting. <https://doi.org/10.48550/arXiv.2003.12140>

Souza, A. N., Wagner, G. L., Ramadhan, A., Allen, B., Churavy, V., Schloss, J., et al. (2020). Uncertainty quantification of ocean parameterizations: Application to the K-profile-parameterization for penetrative convection. *Journal of Advances in Modeling Earth Systems*, 12, e2020MS002108. <https://doi.org/10.1029/2020MS002108>

Stevens, B., Moeng, C.-H., Ackerman, A. S., Bretherton, C. S., Chlond, A., de Roode, S., et al. (2005). Evaluation of large-eddy simulations via observations of nocturnal marine stratocumulus. *Monthly Weather Review*, 133(6), 1443–1462. <https://doi.org/10.1175/MWR2930.1>

Suselj, K., Posselt, D., Smalley, M., Lebsack, M. D., & Teixeira, J. (2020). A new methodology for observation-based parameterization development. *Monthly Weather Review*, 148(10), 4159–4184. <https://doi.org/10.1175/MWR-D-20-0114.1>

Tan, Z., Kaul, C. M., Pressel, K. G., Cohen, Y., Schneider, T., & Teixeira, J. (2018). An extended eddy-diffusivity mass-flux scheme for unified representation of subgrid-scale turbulence and convection. *Journal of Advances in Modeling Earth Systems*, 10(3), 770–800. <https://doi.org/10.1002/2017MS001162>

Tarantola, A. (2005). Inverse problem theory and methods for model parameter estimation. *Society for Industrial and Applied Mathematics*. <https://doi.org/10.1137/1.9780898717921>

Tong, X. T., & Morzfeld, M. (2022). Localization in ensemble Kalman inversion. <https://doi.org/10.48550/arXiv.2201.10821>

van Leeuwen, P. J. (2015). Representation errors and retrievals in linear and nonlinear data assimilation. *Quarterly Journal of the Royal Meteorological Society*, 141(690), 1612–1623. <https://doi.org/10.1002/qj.2464>

Villefranche, N., Blanco, S., Couvreux, F., Fournier, R., Gautrais, J., Hogan, R. J., et al. (2021). Process-based climate model development harnessing machine learning: III. The representation of cumulus geometry and their 3D radiative effects. *Journal of Advances in Modeling Earth Systems*, 13(4), e2020MS002423. <https://doi.org/10.1029/2020MS002423>

Weyn, J. A., Durran, D. R., Caruana, R., & Cresswell-Clay, N. (2021). Sub-seasonal forecasting with a large ensemble of deep-learning weather prediction models. *Journal of Advances in Modeling Earth Systems*, 13(7), e2021MS002502. <https://doi.org/10.1029/2021MS002502>

Xiao, H., Wu, J.-L., Wang, J.-X., Sun, R., & Roy, C. J. (2016). Quantifying and reducing model-form uncertainties in Reynolds-averaged Navier–Stokes simulations: A data-driven, physics-informed Bayesian approach. *Journal of Computational Physics*, 324, 115–136. <https://doi.org/10.1016/j.jcp.2016.07.038>

Zanna, L., & Bolton, T. (2020). Data-driven equation discovery of ocean mesoscale closures. *Geophysical Research Letters*, 47(17), e2020GL088376. <https://doi.org/10.1029/2020GL088376>

Zhao, W. L., Gentine, P., Reichstein, M., Zhang, Y., Zhou, S., Wen, Y., et al. (2019). Physics-constrained machine learning of evapotranspiration. *Geophysical Research Letters*, 46(24), 14496–14507. <https://doi.org/10.1029/2019GL085291>